nature communications

Article

https://doi.org/10.1038/s41467-025-67870-7

TMEM120A maintains adipose tissue lipid homeostasis through ER CoA channeling

Received: 1 July 2025

Accepted: 10 December 2025

Published online: 21 December 2025

Check for updates

Yoon Keun Cho[1,10], Junhyuck Lee[1,10], Yujin L. Jeong[2,10], Minki Shim[3], Xuan Linh Mai[1], Chang Seomoon[1], Cheol Woon Jung[1], Yoon Ha Choi[2], Sik Namgoong[4], Young-Suk Jung[5], Sung Won Kwon[1], Juyong Lee[1], Je Kyung Seong[6], Sunghyouk Park[1], Emilio P. Mottillo[7], James G. Granneman[8], Dong-Kyu Lee[3] ✉, Jong Kyoung Kim[2,9] ✉ & Yun-Hee Lee[1] ✉

Efficient fatty acid (FA) re-esterification is essential for lipid homeostasis in adipocytes, yet the mechanisms coordinating Coenzyme A (CoA) availability at the endoplasmic reticulum (ER)—a major site of lipid synthesis—remain unclear. Here, we identify TMEM120A as an ER-resident CoA-binding protein that regulates intracellular FA metabolism. TMEM120A interacts with the ER-localized acyl-CoA synthetase ACSL1 and ACSL3 to promote long-chain acyl-CoA synthesis and channeling into the ER, thereby facilitating FA re-esterification and lipid cycling during lipolysis. By relieving acyl-CoA-mediated feedback inhibition of lipolysis, TMEM120A enhances lipid turnover while protecting against ER stress and lipotoxicity. Adipocyte-specific deletion of *Tmem120a* in mice impairs lipolysis-induced energy expenditure and exacerbates inflammation and metabolic dysfunction under high-fat diet conditions. These findings establish TMEM120A as a critical regulator of ER CoA handling and lipid flux, revealing a previously unrecognized mechanism that links intracellular CoA dynamics to systemic energy balance and metabolic health.

Adipose tissue plays a central role in energy storage and endocrine regulation, with adipocytes dynamically managing lipid storage and mobilization in response to metabolic cues[1]. During lipolysis, triglycerides (TG) are hydrolyzed into free fatty acids (FFAs) and glycerol to meet energy demands. However, FA mobilization and utilization must be tightly coupled as excessive FAs produce cellular lipotoxicity and ER stress, resulting in systemic metabolic dysfunction[2]. Thus, it is critical that FAs are efficiently channeled into downstream metabolic processes.

FA re-esterification, the process of reincorporating FFAs into TG, acts as a critical buffering mechanism that preserves cellular homeostasis and has been proposed to contribute to energy dissipation via futile lipid cycling[3,4], independent of classical thermogenic mechanisms such as UCP1. Futile lipid cycling involves the coordinated actions of lipolytic enzymes and glycerolipid biosynthetic pathways, enabling continuous TG turnover[3]. Remarkably, up to 85% of FFAs released during lipolysis can be re-esterified[5,6], highlighting the physiological relevance. Beyond buffering FFAs, futile lipid cycling regulates

[1]College of Pharmacy and Research Institute of Pharmaceutical Sciences, Seoul National University, Seoul, Republic of Korea. [2]Department of Life Sciences, Pohang University of Science and Technology (POSTECH), Pohang, Republic of Korea. [3]College of Pharmacy, Chung-Ang University, Seoul, Republic of Korea. [4]Department of Plastic Surgery, Korea University College of Medicine, Seoul, Republic of Korea. [5]College of Pharmacy, Pusan National University, Busan, Republic of Korea. [6]Korea Mouse Phenotyping (KMPC), and Laboratory of Developmental Biology and Genomics, College of Veterinary Medicine, Seoul National University, Seoul, Republic of Korea. [7]Department of Physiology, Wayne State University School of Medicine, Detroit, MI, USA. [8]Center for Molecular Medicine and Genetics, Wayne State University School of Medicine, Detroit, MI, USA. [9]Institute for Convergence Research and Education in Advanced Technology, Yonsei University, Seoul, South Korea. [10]These authors contributed equally: Yoon Keun Cho, Junhyuck Lee, Yujin L. Jeong.
✉e-mail: leedk@cau.ac.kr; blkimjk@postech.ac.kr; yunhee.lee@snu.ac.kr

intracellular lipid intermediates and contributes to processes such as lipid remodeling[7], metabolic signaling[8,9], and thermogenesis[10,11]. Disruption of this tightly regulated cycle has been implicated in obesity, insulin resistance, and non-alcoholic fatty liver disease (NAFLD)[12].

Fatty acid metabolism is initiated by the activation of long-chain fatty acids to acyl-CoA thioester, a reaction catalyzed by acyl-CoA synthetase long-chain (ACSL) family of enzymes. This conversion is essential because in the form of acyl-CoAs can fatty acids be directed toward metabolic fates such as TG synthesis, β-oxidation, phospholipid remodeling, protein acylation, and lipid signaling. Among the five ACSL isoforms, ACSL1 plays a particularly prominent role in adipose tissue. ACSL1-generated acyl-CoAs contribute both to TG synthesis in the ER and to fatty acid oxidation in mitochondria, reflecting its dual function in lipid storage and mitochondrial respiration. The subcellular localization of ACSL1 to the ER and outer mitochondrial membrane provides a mechanism for partitioning acyl-CoAs into distinct metabolic pathways[13]. Accordingly, genetic deletion of ACSL1 in adipose tissue impairs mitochondrial fatty acid oxidation, while also altering lipid storage dynamics[14,15]. In addition, long chain acyl CoAs (LC-acyl-CoAs) suppress lipolysis by binding to adipose triglyceride lipase (ATGL)[13] or its coactivator α-β hydrolase domain containing 5 (ABHD5)[16], highlighting that dynamic and compartmentalized pools of LC-acyl CoA contribute to determining downstream metabolic process.

Despite increasing recognition of the importance of the futile lipid cycling in adipocytes, the molecular mechanisms coordinating local CoA availability and LC-acyl-CoA metabolism are poorly understood. While mitochondrial and peroxisomal CoA transporters have been identified[17,18], how CoA is regulated within the ER, the central site for lipid re-esterification and lipogenesis, has not been elucidated. To date, no ER-specific CoA transporter or channeling mechanism have been reported. Given the compartmentalized nature of acyl-CoA pools and the critical role of the ER in lipid remodeling, identifying proteins that mediate CoA handling at the ER is essential for understanding adipocyte lipid homeostasis. In this study, we investigated the role of transmembrane protein 120 A (TMEM120A), an ER-localized CoA-binding protein, in coordinating organelle-specific CoA trafficking and LC-acyl-CoA metabolism during lipolysis.

TMEM120A shows structural similarity to very long chain fatty acid elongase 7 (ELOVL7)[19–21]. Notably, structural studies revealed a conserved CoA-binding motif within TMEM120A, raising the possibility that it may regulate LC-acyl-CoA metabolism by influencing CoA availability at specific subcellular sites. Given the ER's central role in lipid synthesis and remodeling, proteins that mediate CoA channeling to the ER could be pivotal for re-esterification dynamics.

In this study, we identify TMEM120A as a critical ER-resident CoA-binding protein that coordinates intracellular LC-acyl-CoA metabolism and futile lipid cycling in adipocytes. We show that TMEM120A interacts with ACSL1 and ACSL3 at the ER to facilitate local LC-acyl-CoA generation, promoting FA re-esterification and protecting against lipotoxicity during lipolysis. Adipocyte-specific deletion of TMEM120A impairs β-adrenergic-stimulated lipolysis, disrupts lipid cycling, and worsens metabolic outcomes during high-fat diet (HFD)-induced obesity. These findings reveal TMEM120A as a key regulator of lipid homeostasis with potential therapeutic relevance in metabolic diseases.

Results

Tmem120a is predominantly expressed in adipocytes and downregulated in obesity

We first assessed *Tmem120a* mRNA levels across various mouse tissues and found the highest levels in adipose tissue. (Fig. 1A and Supplementary Fig. 1A). Notably, its expression was higher in WAT than in brown adipose tissue (BAT), at both the mRNA and protein levels (Fig. 1A-C). Furthermore, our single-nucleus RNA sequencing analysis of mouse gonadal white adipose tissue (gWAT) from mice fed a normal chow diet (NCD) revealed that *Tmem120a* mRNA is mainly expressed in adipocytes (Fig. 1D-E). RT-qPCR analysis confirmed that *Tmem120a* mRNA level is predominantly expressed in adipocytes both in inguinal white adipose tissue (iWAT) and gWAT (Fig. 1F). Interestingly, *Tmem120a* expression levels in adipose tissue were reduced in diet-induced obese mouse models (Fig. 1G-I). Consistent with findings from rodent models, *TMEM120A* mRNA level is primarily expressed in adipocytes of human adipose tissue (Fig. 1J), and its expression is significantly reduced in patients with obesity (Fig. 1K). *TMEM120A* expression levels in human adipocytes are negatively correlated with body mass index (BMI) (Fig. 1L-M and Supplementary Fig. 1B-C), highlighting the clinical relevance of our findings. Analysis of publicly available transcriptomic data (Gene Expression Omnibus (GEO): GSE156906) further showed that *TMEM120A* expression is reduced in abdominal subcutaneous WAT of both metabolically-healthy obese (MHO) and metabolically-unhealthy obese (MUO) individuals, compared to metabolically-healthy lean (MHL) individuals (Fig. 1N). In summary, *Tmem120a* is predominantly expressed in adipocytes within adipose tissue, and its expression is decreased in obesity and insulin-resistant states, suggesting a potential role in regulating metabolic health.

TMEM120A is an ER-localized CoA-binding protein lacking fatty acid elongase activity toward C18:0 and C18:3 (n-6)

To investigate the biological function of TMEM120A in adipocytes, we established TMEM120A-overexpressing cell lines using C3H10T1/2 cells. Since TMEM120A expression influences adipogenic differentiation[22], we utilized a doxycycline-inducible cell line to avoid the impact of overexpression (OE) during the differentiation process (Fig. 2A). Doxycycline was administered after adipogenic differentiation and TMEM120A OE was confirmed at both the mRNA and protein levels in C3H10T1/2 adipocytes (Fig. 2B-D).

Using the overexpressing cells, we examined the subcellular localization of TMEM120A in C3H10T1/2 adipocytes by co-staining with markers for the ER (calnexin, PDI), and ER-Tracker), the mitochondria (citrate synthase and MitoTracker), plasma membrane (PM, CellMask^{TM}) and the nuclear envelope (NE, Lamin A/C) (Fig. 2E, Supplementary Fig. 2B, Supplementary Fig. 2D and Supplementary Fig. 2G). GFP- or Myc- tagged TMEM120A showed significant co-localization with the ER, displaying a markedly higher Pearson's coefficient with the ER markers (calnexin, PDI) compared to other markers (Fig. 2F, Supplementary Fig. 2C, Supplementary Fig. 2E, and Supplementary Fig. 2H). We did not detect appreciable levels of TMEM120A at the nuclear rim[22] or plasma membrane[23], previously reported as major sites of localization, suggesting that its subcellular distribution may be context- or cell type-dependent (Fig. 2E, F and Supplementary Fig. 2D-E). To further validate its subcellular localization, we fractionated C3H10T1/2 adipocytes into nuclear, mitochondrial, and ER-enriched microsomal membranes. Consistent with confocal microscopy results, TMEM120A was most abundantly detected in the ER-enriched microsomal fraction (Fig. 2G). Together, these findings indicate that TMEM120A is predominantly localized to the ER in adipocytes.

Given its structural similarity to the FA elongase ELOVL7[19–21] and its ER localization, we investigated potential FA elongation activity of TMEM120A. In vitro FA elongation assay was performed using microsomal fractions from TMEM120A overexpressing HEK293T cells. Incorporation of ^{13}C from malonyl-CoA into elongated FA products was assessed (Fig. 2H), using substrates known to exhibit high activity with ELOVL7—stearoyl-CoA (C18:0) and gamma-linolenoyl-CoA (C18:3, n-6)[24,25]. However, TMEM120A did not exhibit detectable elongation of C18:0-CoA to C20:0-CoA or C18:3 (n-6)-CoA to C20:3 (n-6)-CoA, whereas ELOVL7 showed robust activity (Fig. 2I). These results indicate that TMEM120A lacks catalytic activity for elongating C18:0 and C18:3 (n-6). As previously noted[20], although TMEM120A contains a

https://doi.org/10.1038/s41467-025-67870-7

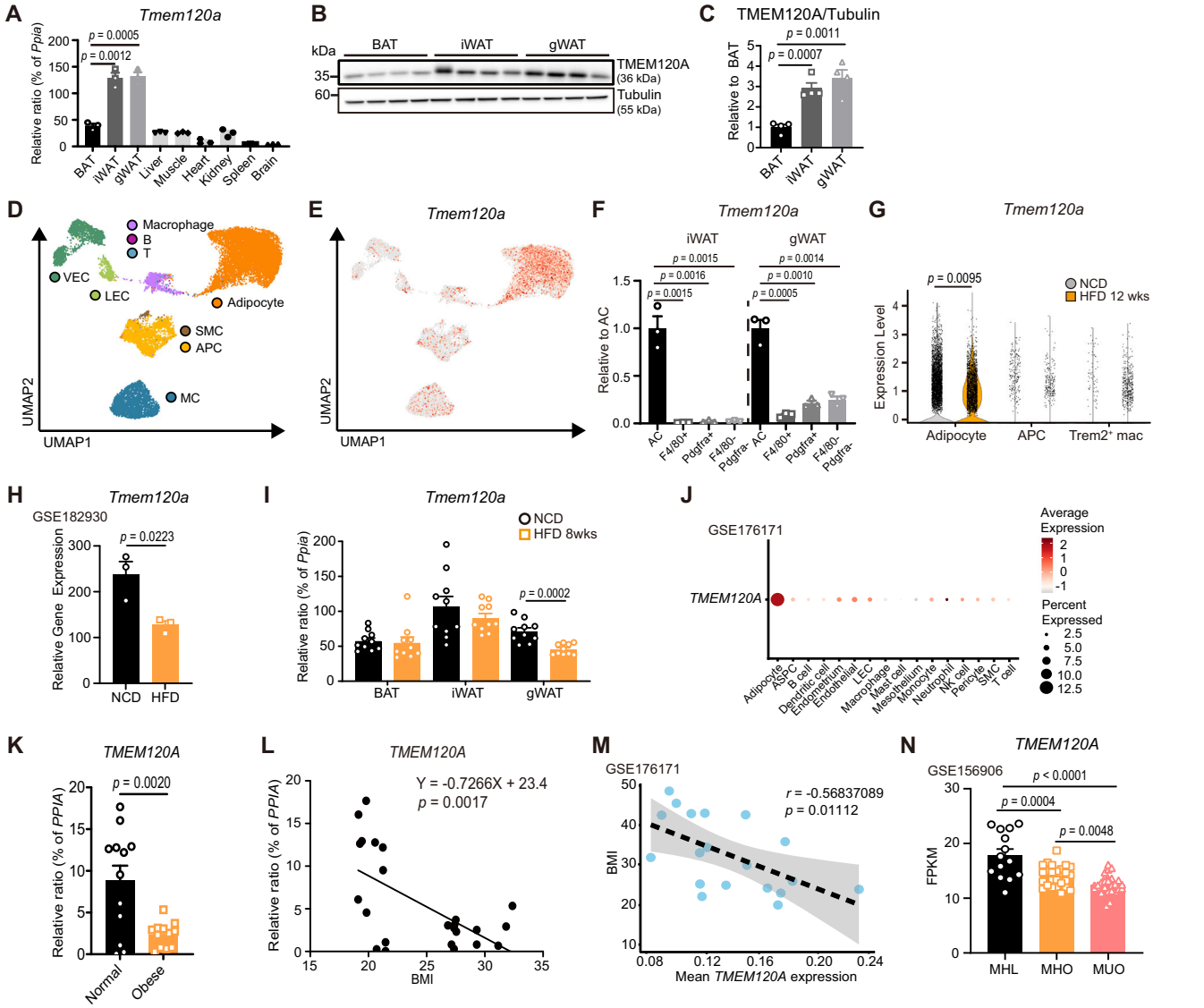

Fig. 1 | *Tmem120a* is predominantly expressed in adipocytes and down-regulated in obesity. A mRNA levels of *Tmem120a* in various tissues. $n = 3$. **B**, **C** Protein expression of TMEM120A in various tissues. $n = 4$. **D**, **E** UMAP plot of total 18,542 nuclei isolated from gWAT of WT and Tmem120a AKO mice fed an NCD. Red color indicates higher expression levels, whereas grey color indicates lower expression levels. (Two replicates for the WT condition and one replicate for the Tmem120a AKO condition). Clusters are colored by cell types: Adipocyte, mesothelial cell (MC), lymphatic endothelial cell (LEC), vascular endothelial cell (VEC), adipocyte progenitor cell (APC), smooth muscle cell (SMC), macrophages, B cell and T cell. **F** mRNA levels of *Tmem120a* in floating adipocytes and F4/80$^+$ macrophages and PDGFRα$^+$ progenitor cells from SVF isolated from iWAT and gWAT. $n = 3$. **G** Single-nucleus RNA analysis of adipocytes, APC, Trem2$^+$ macrophages from gWAT of mice fed an NCD or HFD for 12 weeks (SRP426501). **H** Analysis of *Tmem120a* expression in gWAT of mice fed an NCD or HFD for 8 weeks, determined by publicly available transcriptomic data (GSE182930). $n = 3$. **I** mRNA levels of *Tmem120a* in BAT, iWAT, and gWAT of WT mice fed an NCD or HFD for 8 weeks. $n = 10$. **J** Expression of TMEM120A across different cell types in human white adipose tissue, based on the public dataset GSE176171. Adipose-derived stromal/stem progenitor cell (ASPC). mRNA levels (**K**) and correlation analysis (**L**) of *TMEM120A* gene expression in human subcutaneous adipose tissue of normal (BMI < 22 kg/m^2) and obese (BMI > 26 kg/m^2) patients. $n = 12$. **M** Pearson correlation between BMI and average *TMEM120A* expression in human adipocytes (GSE176171). Each point represents an individual sample. The black dashed line indicates the linear regression fit, and the shaded area represents the 95% confidence interval. **N** Analysis of *TMEM120A* expression in human adipose tissue ((MHL): $n = 14$; (MHO): $n = 25$; (MUO): $n = 27$), determined by publicly available transcriptomic data (GSE156906). Data are presented as mean values ± SEM. Each point represents a biological replicate. p values were determined by an unpaired two-sided Student's t-test (**A, C**, **F**–**I**, **K**, **N**), or two-tailed Pearson correlation (**L**, **M**).

CoA-binding site, it lacks a defined hydrophobic pocket capable of accommodating long-chain fatty acyl chain. To this end, we used AlphaFold3 to model TMEM120A bound to unmodified CoA, palmitoyl-CoA, and oleoyl-CoA. In the TMEM120A–CoA model, the core CoA-binding pocket was predicted with moderate confidence (predicted local distance difference test: pLDDT 70–90, mean ≈85) (Fig. 2J), in keeping with available cryo-EM structures (human WT: PDB 7F3T[20]; mouse H196A/H197A: PDB 7N0L[19]). By contrast, in the palmitoyl-CoA and oleoyl-CoA models, pLDDT scores along the fatty acyl chains declined steadily and fell below 50 at their distal termini (Supplementary Fig. 3). The 16-carbon tail of palmitoyl-CoA even protruded past the putative α-barrel into the solvent-exposed region, while oleoyl-CoA was only forcibly wedged into the pocket by its *cis*-double bond–induced kink (Supplementary Fig. 3). Together, these observations suggest that, although TMEM120A reliably binds the CoA core, it lacks a continuous hydrophobic tunnel to envelop long-chain acyl-CoA substrates, providing a structural rationale for its negligible elongase activity toward C18:0 and C18:3 (n-6).

https://doi.org/10.1038/s41467-025-67870-7

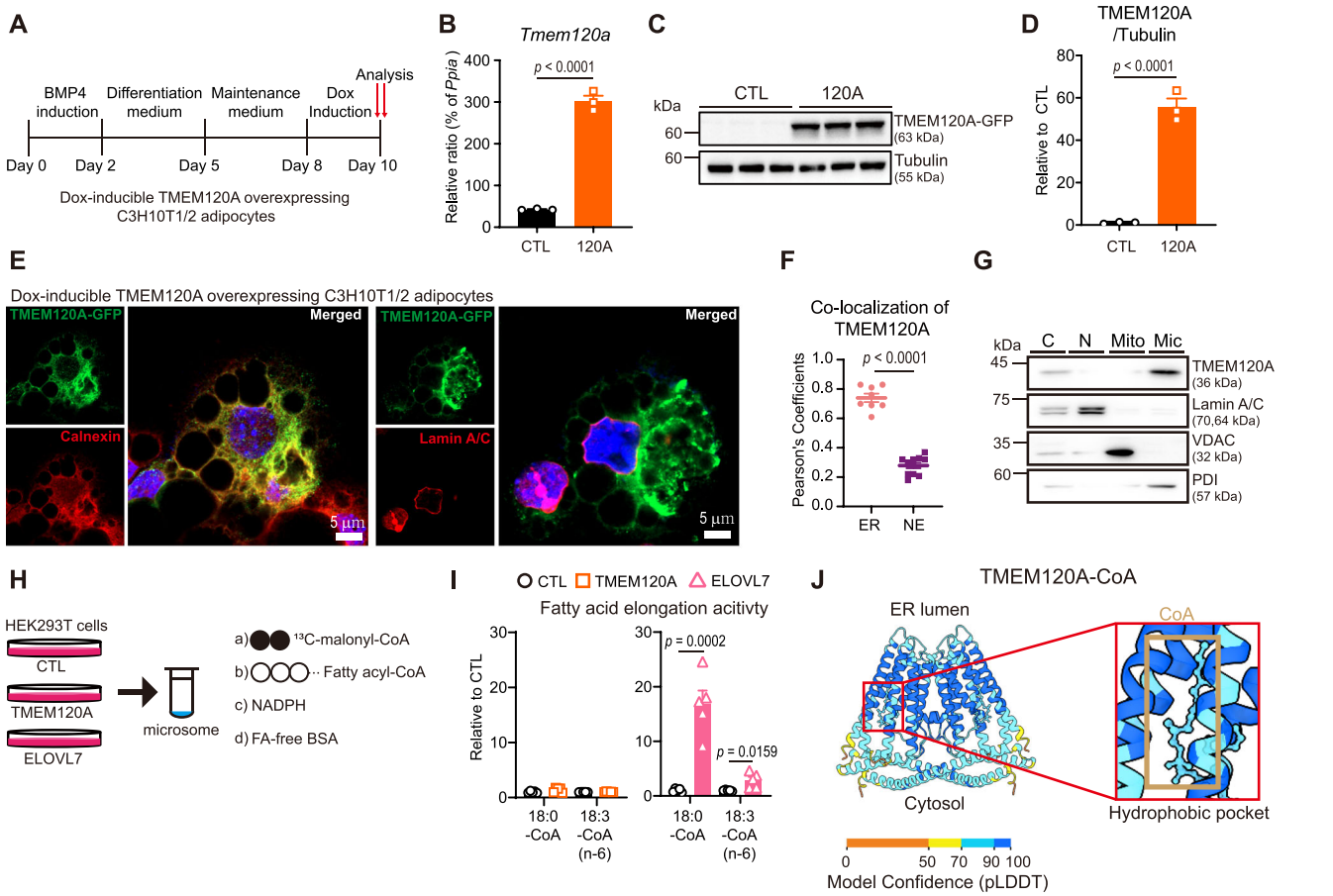

Fig. 2 | TMEM120A is an ER localized CoA-binding protein lacking fatty acid elongase activity. A Schematic diagram representing the generation of doxycycline (Dox)-inducible TMEM120A overexpression model. Confirmation of TMEM120A overexpression model in C3H10T1/2 adipocytes by qPCR (**B**) and immunoblot analysis (**C**, **D**). $n = 3$. **E** Representative images of fixed C3H10T1/2 adipocytes overexpressing GFP-tagged TMEM120A, stained with either anti-Calnexin or anti-Lamin A/C. Nuclei were counterstained with DAPI. $n = 8$. Scale bar, 5 µm. **F** Colocalization analysis of TMEM120A with either anti-Calnexin and anti-Lamin A/C. $n = 8$. **G** Immunoblot analysis of TMEM120A in cell lysate (C), nuclear (N), mitochondrial (Mito), and microsomal (Mic) fractions from C3H10T1/2 adipocytes. Cells were harvested in isolation buffer (IB; 225 mM mannitol, 75 mM sucrose, 0.1 mM EGTA, 30 mM Tris-HCl, pH 7.4) supplemented with protease and phosphatase inhibitors. Adipocytes were homogenized using a syringe. Nuclei were pelleted at 600 x g and lysed in RIPA buffer. The supernatant (containing mitochondria and microsomes) was collected, and crude mitochondria were isolated at 10,000 x g and resuspended in mitochondria resuspending buffer (MRB; 250 mM mannitol, 5 mM HEPES, 0.5 mM EGTA, pH 7.4) supplemented with protease and phosphatase inhibitors. The remaining supernatant (cytosolic fraction containing microsomes) was collected, and microsomal fractions were obtained by ultracentrifugation at 100,000 x g and resuspended in MRB. 3 µg of protein was loaded per lane. **H** Schematic diagram illustrating in vitro fatty acid elongation assay. Microsomal fraction was incubated with 100 µM Tris-HCl (pH 7.4), 200 µM palmitoyl-CoA, 500 µM NADPH, and 60 µM ^{13}C-malonyl-CoA for 1 h. **I** Measurement of in vitro fatty acid elongation activity. $n = 5$. **J**. pLDDT confidence mapping of AlphaFold3–modeled TMEM120A homodimers in complex with CoA. Structures are colored by pLDDT score: 0–50 (orange), 50–70 (yellow), 70–90 (light blue), 90–100 (dark blue). TMEM120A–CoA, the core CoA-binding pocket is predominantly light/dark blue, reflecting high confidence and agreement with cryo-EM data (PDB 7F3T, 7N0L). Data are presented as mean values ± SEM. Each point represents a biological replicate. *p* values were determined by an unpaired two-sided Student's t-test (**B**, **D**, **F**, **I**).

TMEM120A interacts with ACSL1 and ACSL3 at the ER

Previous studies have demonstrated that TMEM120A binds CoA[19–21], and structural modeling using AlphaFold3 further supports stable CoA binding by TMEM120A (Supplementary Table 2). The generation of acyl-CoA is catalyzed by ACSLs, a family of enzymes that activate FFAs by converting them into their CoA derivatives. Among several isoforms, ACSL1 is more abundantly localized to the ER than to mitochondria, but can dynamically translocate to mitochondria to facilitate FA partitioning toward mitochondrial β-oxidation[15,26]. In contrast, ACSL3 is enriched at the ER and lipid droplet (LD) membranes, where it supports FA re-esterification[27–29]. These isoform-specific localizations highlight how compartmentalized acyl-CoA pools regulate FA flux and prevent lipotoxicity[30].

Given that TMEM120A is an ER-resident protein with CoA-binding capability, we hypothesized that TMEM120A might facilitate the utilization of CoA by ACSL1 and ACSL3 for subsequent LC-acyl-CoA production. Supporting this notion, TMEM120A overexpressed in adipocytes co-precipitated endogenous ACSL1 and ACSL3 (Fig. 3A). To evaluate the functional relevance of CoA-binding site in mediating this interaction, we generated a W193A point mutant by substituting the tryptophan residue at position 193, previously identified as critical for CoA binding,[20] with alanine. Interestingly, TMEM120A^{W193A} mutant displayed markedly reduced interaction with ACSL1 and ACSL3, implying that CoA binding is required for the TMEM120A-ACSL1/3 interactions (Fig. 3A). Next, we performed subcellular fractionation to isolate mitochondrial and ER-enriched microsomal fractions, assessing TMEM120A and ACSL1/3 expression in response to increased FA availability. Indeed, isoproterenol stimulation significantly increased the association of TMEM120A, ACSL1, and ACSL3 within the ER-enriched microsomal membranes (Fig. 3B-E). To further examine whether TMEM120A regulates ACSL1/3 localization at the ER, we analyzed ACSL1/3 distribution in *Tmem120a* knockdown (KD) C3H10T1/2

https://doi.org/10.1038/s41467-025-67870-7

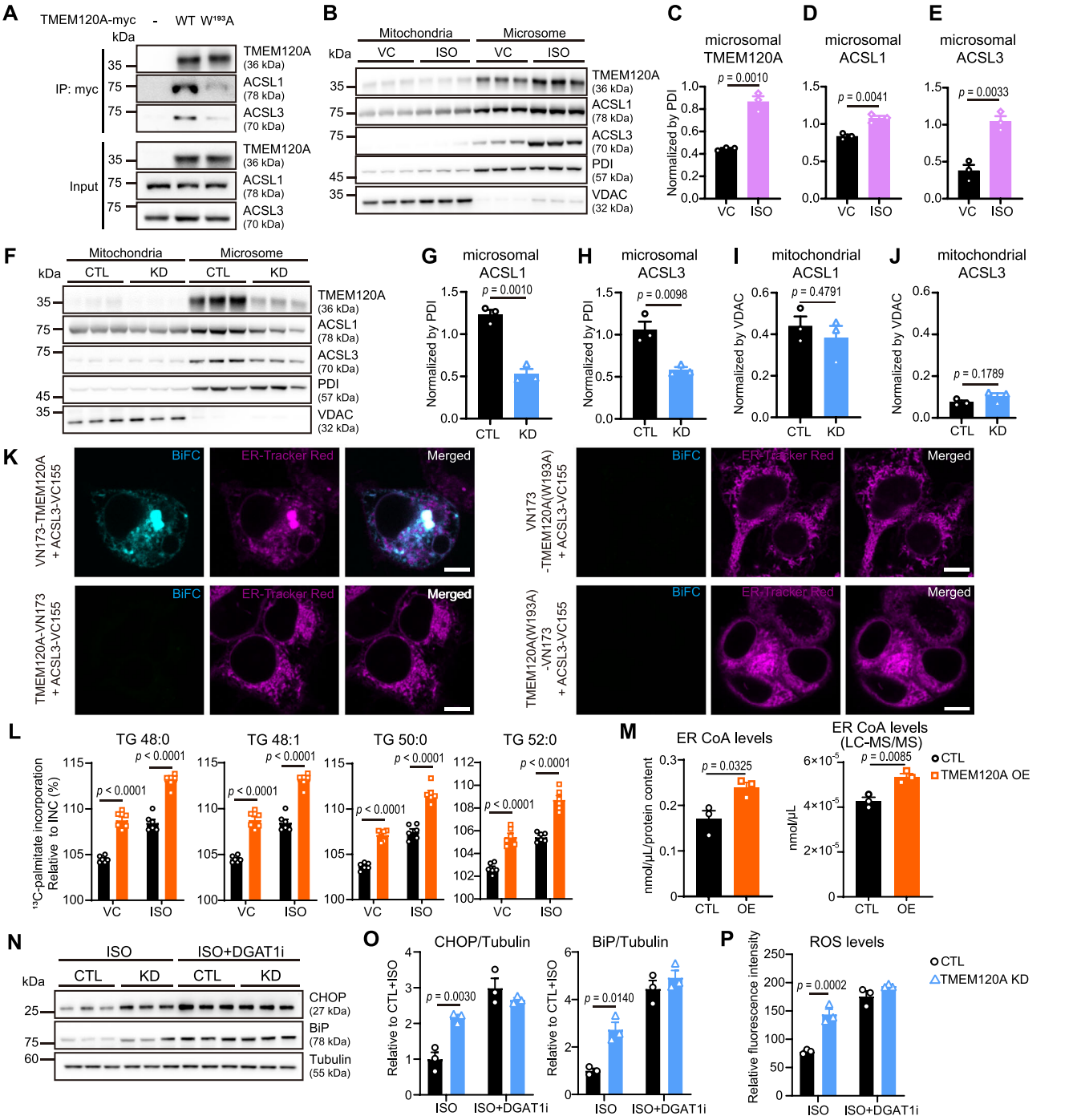

Fig. 3 | TMEM120A physically interacts with ACSL1 and ACSL3 at the ER and enhances fatty acid re-esterification. A IP analysis with control and overexpressed TMEM120A^{WT} or TMEM120A^{W193A} and endogenous ACSL1 or ACSL3 of C3H10T1/2 adipocytes. **B**–**E** Immunoblot analysis of ACSL1, ACSL3 and TMEM120A in mitochondrial and microsomal fraction of C3H10T1/2 adipocytes treated with either vehicle control (VC) or isoproterenol (ISO) for 2 h. $n = 3$. **F**–**J** Immunoblot analysis of ACSL1, ACSL3 and TMEM120A in mitochondrial and microsomal fraction of control or *Tmem120a* knockdown C3H10T1/2 adipocytes. $n = 3$. **K** Bimolecular fluorescence complementation (BiFC) analysis of TMEM120A and ACSL3 in HEK293T cells. BiFC signals are shown in green, while ER-Tracker Red is shown in red. BiFC signals correspond to ER stained with ER-Tracker Red. $n = 5$. Scale bar, 10 μm. **L** Assessment of fatty acid re-esterification rates by measuring ^{13}C-palmitate incorporation into triacylglycerol (TG) species in C3H10T1/2 adipocytes overexpressing TMEM120A or control cells. Cells were treated with either VC or ISO (10 μM) and ^{13}C-palmitate (100 μM) for 2 h. Data are presented relative to the isotope negative control (INC, %), in which cells were incubated with unlabeled palmitate (100 μM). $n = 6$. **M** Quantification of CoA levels in ER-enriched microsomal fractions from C3H10T1/2 adipocytes overexpressing TMEM120A or control cells, using an enzymatic kit and targeted LC-MS/MS. $n = 3$. **N**, **O** Immunoblot analysis of ER stress markers in controls or *Tmem120a* knockdown C3H10T1/2 adipocytes treated with A922500 (DGAT1 inhibitor, 5 μM) for 1 h, followed by treating with ISO (10 μM) for 4 h. $n = 3$. **P** Measurement of ROS levels using H_2DCFDA (10 uM) in controls or *Tmem120a* knockdown C3H10T1/2 adipocytes treated with either vehicle or A922500 (DGAT1 inhibitor, 5 μM) for 1 h, followed by treating with ISO (10 μM) for 4 h. $n = 3$. Data are presented as mean values ± SEM. Each point represents a biological replicate. *p* values were determined by a two-way ANOVA followed Sidak's multiple comparisons test (**C**–**E**, **G**–**J**, **L**, **O**, **P**) and an unpaired two-sided Student's t-test (**M**).

adipocytes. TMEM120A deficiency reduced levels of ER-localized ACSL1/3, with no corresponding change in their mitochondrial localization, indicating that TMEM120A contributes to the retention of ACSL1/3 at the ER (Fig. 3F-J). To map interaction geometry, we performed bimolecular fluorescence complementation (BiFC). Based on predictions that the N-terminal hydrophobic region of ACSL3 forms a transmembrane domain[28] and both the N- and C- terminal ends of TMEM120A are oriented toward the cytosol[20], we tested ACSL3-VC155 (C-terminal VC155 fusion) with TMEM120A fused to Venus at either the N terminus (VN173-TMEM120A) or the C terminus (TMEM120A-VN173). BiFC signal was detected exclusively at the ER when VN173-TMEM120A was co-expressed with ACSL3-VC155, indicating that C-terminal TMEM120A and N-terminal ACSL3 interactions are orientation dependent. Notably, the TMEM120A^{W193A} mutant abolished the BiFC signal, underscoring the requirement of W193/CoA binding for the TMEM120A–ACSL3 interaction (Fig. 3K). Collectively, these findings identify TMEM120A as a CoA-binding ER membrane protein that interacts with ACSL1 and ACSL3 and promotes their ER association in a CoA-binding–dependent and orientation-dependent manner.

TMEM120A promotes fatty acid re-esterification and mitigates lipotoxic ER stress during lipolysis

Next, we examined the impact of TMEM120A overexpression and *Tmem120a* KD on FA re-esterification during lipolysis by tracing the ^{13}C-palmitate incorporation into TG species, with incorporation rates compared to those obtained using unlabeled ^{12}C-palmitate as an isotope negative control. At the basal level, TMEM120A overexpression enhanced the ^{13}C-palmitate incorporation into TGs including 48:0, 48:1, 50:0, and 52:0, while *Tmem120a* KD reduced ^{13}C-palmitate re-esterification into TGs (Fig. 3L and Supplementary Fig. 4A). Isoproterenol treatment further increased ^{13}C-palmitate incorporation, indicating that lipolytic stimulation promotes FA re-esterification (Fig. 3L and Supplementary Fig. 4A). TMEM120A overexpression under isoproterenol stimulated conditions similarly elevated ^{13}C-palmitate incorporation into the same TG species, whereas *Tmem120a* KD decreased ^{13}C-labeled TGs (Fig. 3L and Supplementary Fig. 4A). In contrast, ^{13}C-palmitate incorporation into phosphatidylcholine (PC) species such as 32:0, 34:0, and 34:1 PCs was unaffected by TMEM120A overexpression (Supplementary Fig. 5A-C). Notably, isoproterenol treatment reduced ^{13}C-palmitate incorporation into PCs (Supplementary Fig. 5A-C), suggesting a preferential metabolic shift toward TG synthesis during lipolysis. To assess whether the role of TMEM120A is specific to the ER, we quantified CoA levels in ER-enriched microsomal fractions. TMEM120A OE increased ER CoA levels, whereas *Tmem120a* KD decreased them, supporting an ER-associated role for TMEM120A in CoA handling (Fig. 3M and Supplementary Fig. 4B).

To test whether TMEM120A affects mitochondrial function, we measured oxygen consumption rate (OCR) in C3H10T1/2 adipocytes. Basal and maximal respirations were unchanged between control and *Tmem120a* KD cells, indicating intact mitochondrial oxidative capacity. In contrast, isoproterenol-stimulated OCR was attenuated in *Tmem120a* KD cells, consistent with reduced lipolytic flux and lower ATP demand due to diminished FA/TG cycling (Supplementary Fig. 6A-D). We also evaluated the expression levels of mitochondrial proteins, including cytochrome c oxidase subunit 4 (COXIV) and medium-chain acyl-CoA dehydrogenase (MCAD), following *Tmem120a* KD. Protein and mRNA levels remained unchanged under both basal and isoproterenol-stimulated conditions (Supplementary Fig. 6E-G).

Previous studies have proposed that the re-esterification cycle mitigates lipotoxic stress rather than preserving TG mass[31]. In light of this, we investigated whether *Tmem120a* KD provokes ER stress due to impaired re-esterification of FFAs into TG. Under isoproterenol-stimulated conditions, *Tmem120a* KD elevated ER stress markers, including BiP and CHOP (Fig. 3N-O). Pharmacological inhibition of DGAT1, which blocks FA re-esterification, further exacerbated ER stress in control cells, but had no additional effect in *Tmem120a* KD cells, indicating that defective FA re-esterification is the principal driver of ER response (Fig. 3N-O). ER stress is known to elevate reactive oxygen species (ROS) by disrupting protein folding and redox balance in the ER[32]. Consistent with this, *Tmem120a* KD increased ROS levels upon lipolytic stimulation, whereas DGAT1 inhibition did not further enhance ROS levels in *Tmem120a* KD cells (Fig. 3P).

Collectively, these findings demonstrate that TMEM120A promotes FA flux into the ER during lipolysis. By contributing to ER CoA availability, possibly through recycling CoA in ER, TMEM120A may facilitate LC-acyl-CoA formation and support FA re-esterification in the ER, thereby helping to maintain intracellular lipid homeostasis. Furthermore, the loss of TMEM120A impairs FA re-esterification, leading to ER stress and subsequent oxidative stress.

TMEM120A sustains lipolysis by alleviating LC-acyl-CoA–mediated feedback inhibition in adipocytes

During lipolysis, LC-acyl-CoAs are generated and subsequently directed toward either re-esterification or β-oxidation. Cytosolic LC-acyl-CoAs also act as negative feedback regulators by binding directly to ATGL[13] or its coactivator ABHD5[16]. Based on these findings, we hypothesized that enhancing the utilization of LC-acyl-CoA through re-esterification in the ER would reduce cytosolic LC-acyl-CoA levels. To test this, we monitored cytosolic LC-acyl-CoA dynamics in TMEM120A-overexpressing adipocytes during lipolysis utilizing a single-molecule (intramolecular) fluorescence resonance energy transfer (FRET) sensor[33] in cells overexpressing TMEM120A or control (Fig. 4A). The sensor consists of a cyan fluorescent protein (CFP) mutant fused to ABHD5, followed by a flexible linker composed of GGS repeats, yellow fluorescent protein (YFP), and PLIN5$^{384\text{-}417}$, and is designed to report LC-acyl-CoA-induced ABHD5-PLIN5 interaction. The FRET sensor utilizes CFP and YFP mutants with weak dimerization properties; under elevated LC-acyl-CoA conditions, the interaction between PLIN5$^{384\text{-}417}$ and ABHD5 is enhanced, thereby disrupting the weak intramolecular interaction between CFP and YFP and resulting in a reduction in FRET efficiency. We introduced the FRET sensor into C3H10T1/2 cells and confirmed its localization to the surface of LDs (Supplementary Fig. 7). To assess sensor responsiveness, cells were treated with isoproterenol to induce lipolysis and promote endogenous LC-acyl-CoA production. As expected, isoproterenol treatment significantly increased lipolysis-derived LC-acyl-CoA levels as reflected by reduced FRET (Fig. 4B, C). In contrast, TMEM120A overexpression significantly attenuated the isoproterenol-induced reduction in the FRET ratio (Fig. 4B, C), indicating a decreased cytosolic LC-acyl-CoA levels. Importantly, overexpression of TMEM120A^{W193A} mutant abolished the inhibitory effect of TMEM120A on the isoproterenol-induced decrease in the FRET ratio, highlighting the critical role of this residue in regulating intracellular LC-acyl-CoA levels (Fig. 4B, C).

Next, we examined whether TMEM120A-mediated reduction in cytosolic LC-acyl-CoA levels modulates lipolysis through a negative feedback mechanism in adipocytes. Isoproterenol treatment significantly elevated the phosphorylation of HSL at Ser660 and PLIN1 at Ser517–downstream targets of protein kinase A (PKA) activation in TMEM120A overexpressing C3H10T1/2 adipocytes (Fig. 4D, E). Consistently, intracellular cyclic adenosine monophosphate (cAMP) levels, which drive PKA activation, were significantly elevated by TMEM120A overexpression, indicating that TMEM120A modulates processes upstream of cAMP signaling (Fig. 4F). Correspondingly, lipolytic activity, measured by the release of FFAs and glycerol, was markedly elevated by TMEM120A overexpression (Fig. 4G, H). In contrast, TMEM120A^{W193A} mutant did not elicit a comparable increase, underscoring the importance of CoA-binding site in modulating lipolysis via regulation of LC-acyl-CoA metabolism (Fig. 4G, H).

In addition to isoproterenol treatment, we utilized SR-3420, an ABHD5 ligand that activate ATGL-mediated lipolysis independent of

https://doi.org/10.1038/s41467-025-67870-7

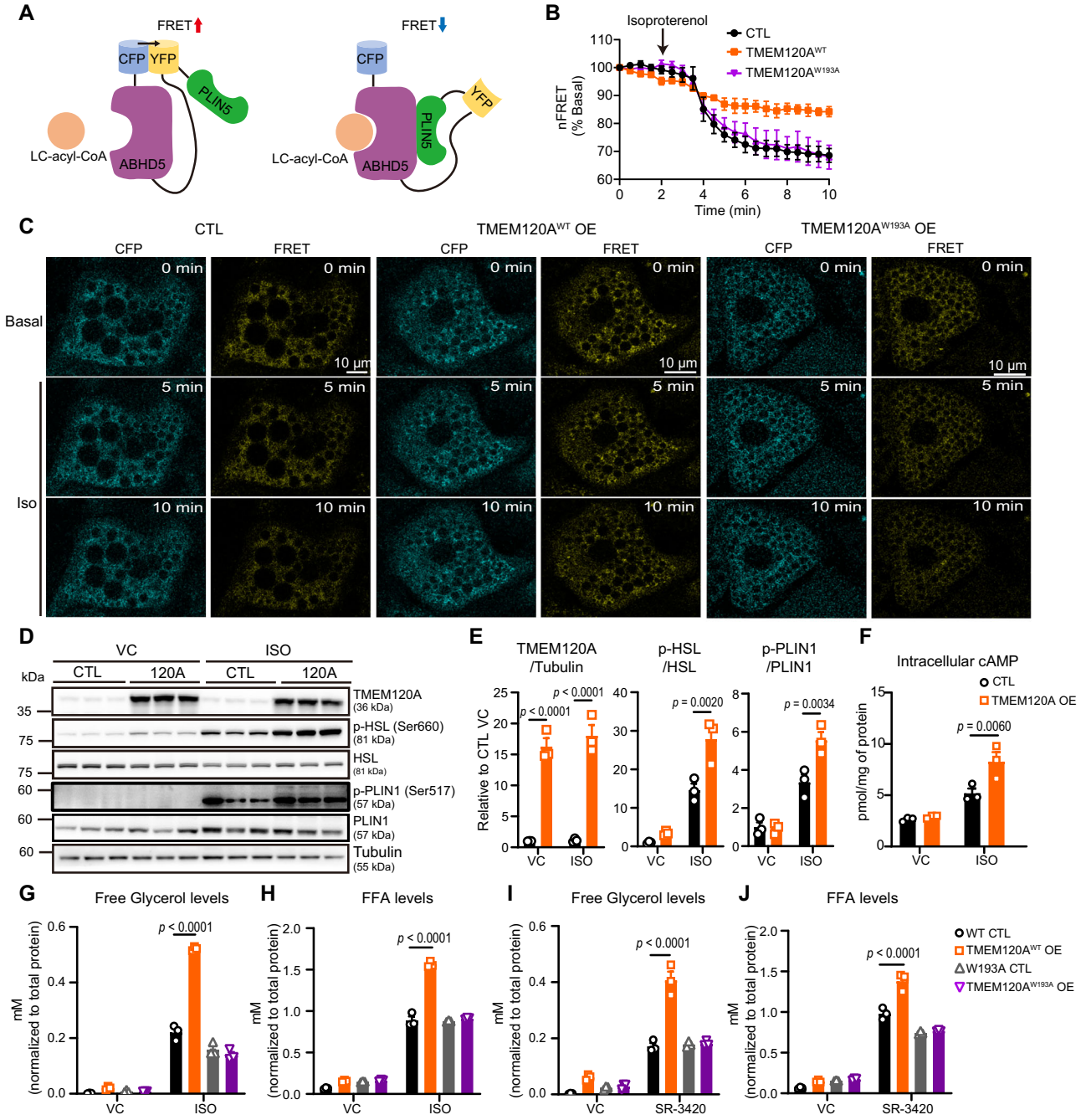

Fig. 4 | TMEM120A promote lipolysis by reducing cytosolic LC-acyl-CoA levels in adipocytes. A Schematic of the single-molecule FRET sensor containing Cerulean (CFP) mutant in fusion with ABHD5, a flexible region containing GGS repeats (black line), Citrine (YFP), and PLIN5$^{384-417}$. **B** C3H10T1/2 adipocytes stably expressing the ABHD5^{R299N} LC-acyl-CoA sensor and TMEM120A (WT or W193A mutant) or ABHD5^{R299N} LC-acyl-CoA sensor alone were imaged using laser scanning confocal microscopy at 30-second interval. Isoproterenol (ISO) was treated at the indicated time, and the nFRET signals were calculated. $n = 4$. Data are from four independent experiments imaged for each condition and are representative of 4 individual experiments. **C** Confocal imaging of C3H10T1/2 adipocytes stably expressing the ABHD5^{R299N} LC-acyl-CoA sensor and TMEM120A (WT or W193A mutant) or ABHD5^{R299N} LC-acyl-CoA sensor alone at the indicated time. Scale bar, 10 μm. $n = 4$. **D**, **E** Immunoblot analysis of TMEM120A overexpressing C3H10T1/2 adipocytes or controls treated with either vehicle control (VC) or ISO (10 μM) for 4 h. $n = 3$. **F** Intracellular cAMP levels in TMEM120A overexpressing C3H10T1/2 adipocytes or controls treated with either VC or ISO (10 μM) for 4 h. $n = 3$. Glycerol (**G**) and FFA (**H**) in the treatment media following 4 h treatment with ISO in TMEM120A (WT or W193A mutant) overexpressing C3H10T1/2 adipocytes or controls. $n = 3$. Glycerol (**I**) and FFA (**J**) in the treatment media following 4 h treatment of either VC or SR-3420 (20 μM) in TMEM120A (WT or W193A mutant) overexpressing C3H10T1/2 adipocytes or controls. $n = 3$. Data are presented as mean values ± SEM. Each point represents a biological replicate. p values were determined by a two-way ANOVA followed Sidak's multiple comparisons test (**E**–**J**).

PKA[34], by directly releasing ABHD5 from PLIN1. Similar to isoproterenol-induced lipolysis, TMEM120A overexpression further increased lipolytic activity in the presence of SR-3420, whereas TMEM120A^{W193A} mutant exhibited no synergistic effects (Fig. 4I, J). This finding indicates that TMEM120A regulates subcellular distribution of LC-acyl-CoAs, thereby reducing negative feedback on lipolytic enzyme activity. Taken together, these results demonstrate that TMEM120A overexpression enhances lipolysis as well as

https://doi.org/10.1038/s41467-025-67870-7

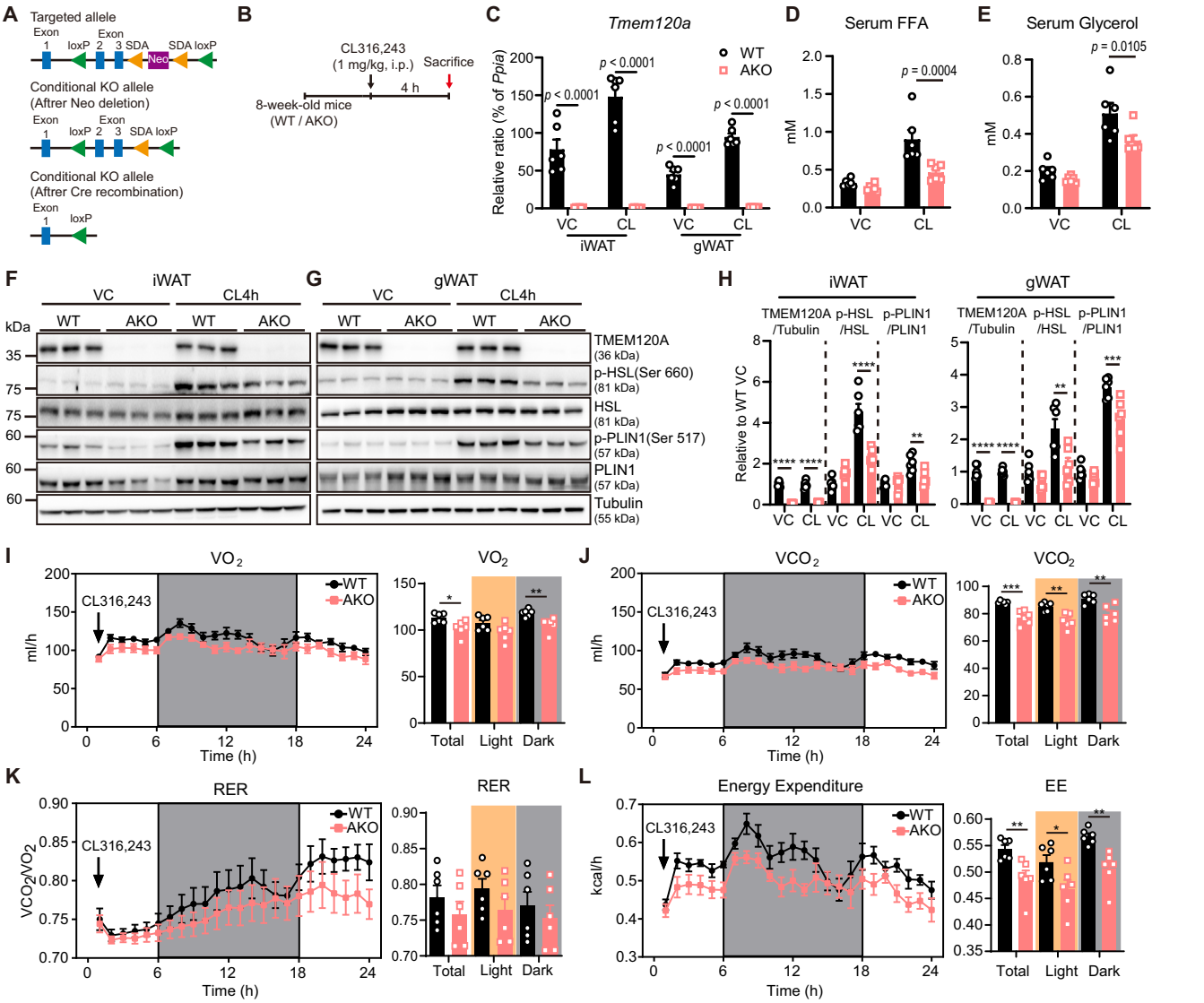

Fig. 5 | Adipocyte-specific deletion of TMEM120A impairs CL-induced lipolysis and reduces energy expenditure in vivo. A Schematic diagram showing the establishment of adipocyte-specific TMEM120A KO mice (TMEM120A AKO). Male mice at 8 weeks of age were used for the experiments. **B** Experimental design of WT and TMEM120A AKO mice at 8 weeks of age treated intraperitoneally with CL316,243 (1 mg/kg) for 4 h. **C** mRNA levels of *Tmem120a* in adipose tissues of WT and TMEM120A AKO mice treated with either vehicle control (VC) or CL316,243 (CL). $n = 6$. FFA (**D**) and glycerol (**E**) in serum of WT and TMEM120A AKO mice treated with either VC or CL for 4 h. $n = 6$. **F**–**H** Immunoblot analysis of iWAT and gWAT of WT and TMEM120A AKO mice treated with either VC or CL for 4 h. $n = 6$. Significant effects of genotype in protein levels of iWAT (TMEM120A/Tubulin: VC:WT vs. VC:AKO, $p < 0.0001$; CL:WT vs. CL:AKO, $p < 0.0001$; p-HSL/HSL: CL:WT vs. CL:AKO, $p < 0.0001$; p-PLIN/PLIN: CL:WT vs. CL:AKO, $p = 0.0094$) Significant effects of genotype in protein levels of gWAT (TMEM120A/Tubulin: VC:WT vs. VC:AKO, $p < 0.0001$; CL:WT vs. CL:AKO, $p < 0.0001$; p-HSL/HSL: CL:WT vs. CL:AKO, $p = 0.0047$; p-PLIN/PLIN: CL:WT vs. CL:AKO, $p = 0.0012$) **I-L.** Indirect calorimetry analysis. Arrows indicate the injection of CL. VO_2: rate of oxygen consumption; VCO_2: rate of carbon dioxide production; RER: respiratory exchange ratio. $n = 6$. Significant effects of genotype in VO_2 (Total VO_2, $p = 0.0189$; Dark VO_2, $p = 0.0047$). Significant effects of genotype in VCO_2 (Total VCO_2, $p = 0.0004$; Light VCO_2, $p = 0.0018$; Dark VCO_2, $p = 0.0027$). Significant effects of genotype in EE (Total EE, $p = 0.0081$; Light EE, $p = 0.0387$; Dark EE, $p = 0.0023$). Data are presented as mean values ± SEM. Each point represents a biological replicate. p values were determined by an unpaired two-sided Student's t-test (**I**–**L**) or a two-way ANOVA followed Sidak's multiple comparisons test (**C**–**E**, **H**).

re-esterification of LC-acyl-CoA, thereby contributing to the facilitation of lipid cycling.

Adipocyte-specific deletion of TMEM120A impairs CL-induced lipolysis and reduces energy expenditure in vivo

To investigate the physiological role of TMEM120A in adipose tissue in vivo, we generated adipocyte-specific TMEM120A knockout (TMEM120A AKO) model by crossing *Tmem120a*$^{flox/flox}$ (*Tmem120a*$^{fl/fl}$) mice with Adipoq-Cre mice (Fig. 5A). We assessed *Tmem120a* mRNA levels and confirmed its depletion in iWAT and gWAT (Fig. 5B). TMEM120A shares a paralog, transmembrane 120B (TMEM120B), with approximately 70% amino acid sequence identity (Supplementary Fig. 8A). Thus, we examined whether TMEM120A AKO affects the compensatory upregulation of its paralog. RT-qPCR and immunoblot analysis confirmed that the mRNA and protein levels of TMEM120B, a paralog of TMEM120A, is not affected by the loss of *Tmem120a* (Supplementary Fig. 8B-F). TMEM120A expression levels in adipose tissue were comparable between male and female mice across all depots, which contrasts with previously reported findings[35] (Supplementary Fig. 8G-I). Under normal chow diet conditions, TMEM120A deficiency did not result in any overt morphological or functional abnormalities during developmental growth or at baseline. To further assess whether

TMEM120A possesses fatty acid elongase activity in vivo and whether its deficiency alters fatty acid chain length or composition, we performed fatty acid methyl ester analysis using gas chromatography-mass spectrometry (GC-MS). This analysis revealed no significant differences in fatty acid profiles across all examined adipose depots between wild type (WT) and TMEM120A AKO mice (Supplementary Fig. 9).

Building on in vitro findings that TMEM120A overexpression enhances lipolysis in C3H10T1/2 adipocytes, we next evaluated the effect of TMEM120A AKO on CL316,243-induced lipolysis in vivo (Fig. 5A-C). We hypothesized that TMEM120A AKO reduces the capacity to sequester LC-acyl-CoA, resulting in enhanced LC-acyl-CoA-mediated negative feedback. Consistent with our hypothesis, circulating levels of FFA and glycerol were significantly lower in TMEM120A AKO mice after CL316,243 treatment (Fig. 5D, E). Additionally, immunoblot analysis demonstrated reduced phosphorylation levels of HSL at Ser660 and PLIN1 at Ser517 in iWAT and gWAT of TMEM120A AKO mice following CL316,243 treatment (Fig. 5F-H). Next, we investigated whether the impaired lipolytic activity observed upon CL316,243 treatment affects systemic energy metabolism. Following CL316,243 injection, TMEM120A AKO mice exhibited a significant attenuation of CL316,243-induced increases in VO_2, VCO_2 and energy expenditure (Fig. 5I, J and L), while respiratory exchange ratio (RER) remained unchanged compared to WT controls (Fig. 5K). Consistently, TMEM120A KO attenuated CL316,243-induced fat loss (Supplementary Fig. 10A-B). Collectively, these findings indicate that the absence of TMEM120A suppresses β3-adrenergic activation of lipolysis and energy expenditure.

Adipocyte-specific deletion of TMEM120A induces transcriptional signatures associated with oxidative stress and inflammation, without affecting systemic metabolic parameters

To further characterize transcriptional changes, we analyzed gene expression profiles in representative adipose depots obtained from WT and TMEM120A AKO mice: gWAT via single-nucleus RNA sequencing and BAT via bulk RNA sequencing. We analyzed mice at 20 weeks of age to capture potential cumulative effects of aging on gene expression that may have been undetectable at an earlier time point (i.e. 8 weeks) (Fig. 6A and Supplementary Fig. 11A). Using a graph-based clustering algorithm, nuclei were grouped into distinct clusters and annotated into 9 cell types based on curated gWAT-specific marker gene expression (Supplementary Fig. 11B). Differential gene expression analysis revealed that TMEM120A deletion in adipocytes significantly downregulated genes involved in lipid metabolism and insulin signaling. In contrast, genes associated with ER stress, peroxisomal function, ROS response, and oxidative phosphorylation were markedly upregulated in TMEM120A-deficient adipocytes (Fig. 6B). Gene ontology (GO) and KEGG (Kyoto Encyclopedia of Genes and Genomes) pathway enrichment analyses further demonstrated that transcriptional programs associated with mitochondrial matrix organization, ROS response, responsive to oxidative stress, oxidative phosphorylation, and peroxisome were significantly enriched in TMEM120A-deficient adipocytes (Fig. 6C). Conversely, pathways related to insulin stimulus, insulin receptor signaling pathway, TG biosynthetic process, lipid storage, and positive regulation of lipid biosynthetic process were significantly downregulated (Fig. 6D), suggesting impaired insulin sensitivity and lipid anabolic capacity. Supporting these findings, violin plots showed increased module scores for peroxisome biogenesis and peroxisomal β-oxidation in TMEM120A-deficient adipocytes (Fig. 6E). Next, Gene set enrichment analysis (GSEA) revealed strong enrichment of gene sets related to oxidative stress, detoxification of reactive oxygen species, and myeloid leukocyte activation (Fig. 6F) along with a significant increase in TNFα pathway (Fig. 6G) in macrophages from gWAT of TMEM120A AKO mice, indicating the presence of intracellular stress and pro-inflammatory cues. Additionally, stromal cell populations including vascular endothelial cells, lymphatic endothelial cells, and mesothelial cells from TMEM120A AKO mice exhibited inflammatory gene signatures, including TNFα signaling via NF-kB, apoptosis, and oxidative stress response (Fig. 6H). RT-qPCR analysis of gWAT from TMEM120A AKO mice revealed elevated expression of genes involved in oxidative phosphorylation (*Cox7c*, *Atp5a1*), and oxidative stress (*Ftl1*, *Fth1*, *Hif1a*). In contrast, genes associated with the insulin signaling and glucose uptake (*Slc2a4*) and adipocyte-specific markers (*Plin1*, *Fabp4*) were downregulated compared with WT controls (Fig. 6I). Taken together, dysregulated intracellular LC-acyl-CoA flux in TMEM120A AKO leads to impaired lipid metabolism and insulin signaling. This perturbation concurrently induces compensatory transcriptional programs, including oxidative phosphorylation, peroxisomal biogenesis and peroxisomal β-oxidation, likely to enhance the utilization of cytosolic LC-acyl-CoAs. However, the upregulation of peroxisomal fatty acid oxidation contributes to ROS accumulation and activation of oxidative stress response pathways in adipocytes, accompanied by enhanced inflammatory signaling in stromal cell populations.

Bulk RNA-seq analysis of BAT revealed that a total of 418 genes were significantly downregulated, while 97 genes were upregulated ($|\text{fold change}| \geq 2$, raw $p < 0.05$) in TMEM120A AKO mice compared to WT mice (Supplementary Fig. 12A). Pathway enrichment analysis using the KEGG database revealed that the upregulated genes were significantly enriched in immune-related pathways, including viral protein interaction with cytokine and cytokine receptors, cytokine–cytokine receptor interactions, IL-17 signaling, and chemokine signaling (Supplementary Fig. 12B). GO analysis of the upregulated genes showed significant enrichment for molecular functions such as chemokine activity and CCR chemokine receptor binding (Supplementary Fig. 12C), as well as biological processes related to the positive regulation of cell migration, inflammatory response, signal transduction, chemokine-mediated signaling, and eosinophil chemotaxis (Supplementary Fig. 12D). These findings suggest that TMEM120A deficiency promotes a transcriptional program characterized by enhanced inflammatory signaling, chemokine-mediated pathways, and immune cell recruitment.

To evaluate the physiological impact of TMEM120A deficiency on systemic energy balance, we performed indirect calorimetry in WT and TMEM120A AKO mice at 20 weeks of age. Despite observing alteration in transcript levels at the single-cell and tissue levels, no significant differences in VO_2, VCO_2, RER, and energy expenditure were observed between genotypes (Supplementary Fig. 13A-D). Additionally, locomotor activity and food intake were comparable between WT and TMEM120A AKO mice (Supplementary Fig. 13E-F). In support of these findings, adipose tissue depot weights did not differ significantly between genotypes (Fig. 6J), and both fat mass and lean mass remained unchanged (Fig. 6K). Furthermore, fasting glucose levels and glucose tolerance tests revealed no significant differences between WT and TMEM120A AKO mice, indicating preserved glucose homeostasis between the genotypes (Fig. 6L and Supplementary Fig. 13G). Collectively, these findings demonstrate that, despite transcriptional changes at the single-cell level, TMEM120A deficiency does not impact whole-body energy metabolism under basal conditions up to 20 weeks of age.

Loss of adipocyte TMEM120A exacerbates obesity-driven metabolic impairments

Although transcriptomic alterations were observed in both BAT and gWAT of TMEM120A AKO mice at 20 weeks of age, these changes did not translate into altered energy expenditure or impaired glucose homeostasis. To further assess the functional relevance of these transcriptional changes, we next subjected WT and TMEM120A AKO mice to a HFD for 12 weeks (Fig. 7A). This approach aimed to evaluate the impact of TMEM120A deficiency on pathological adipose tissue

https://doi.org/10.1038/s41467-025-67870-7

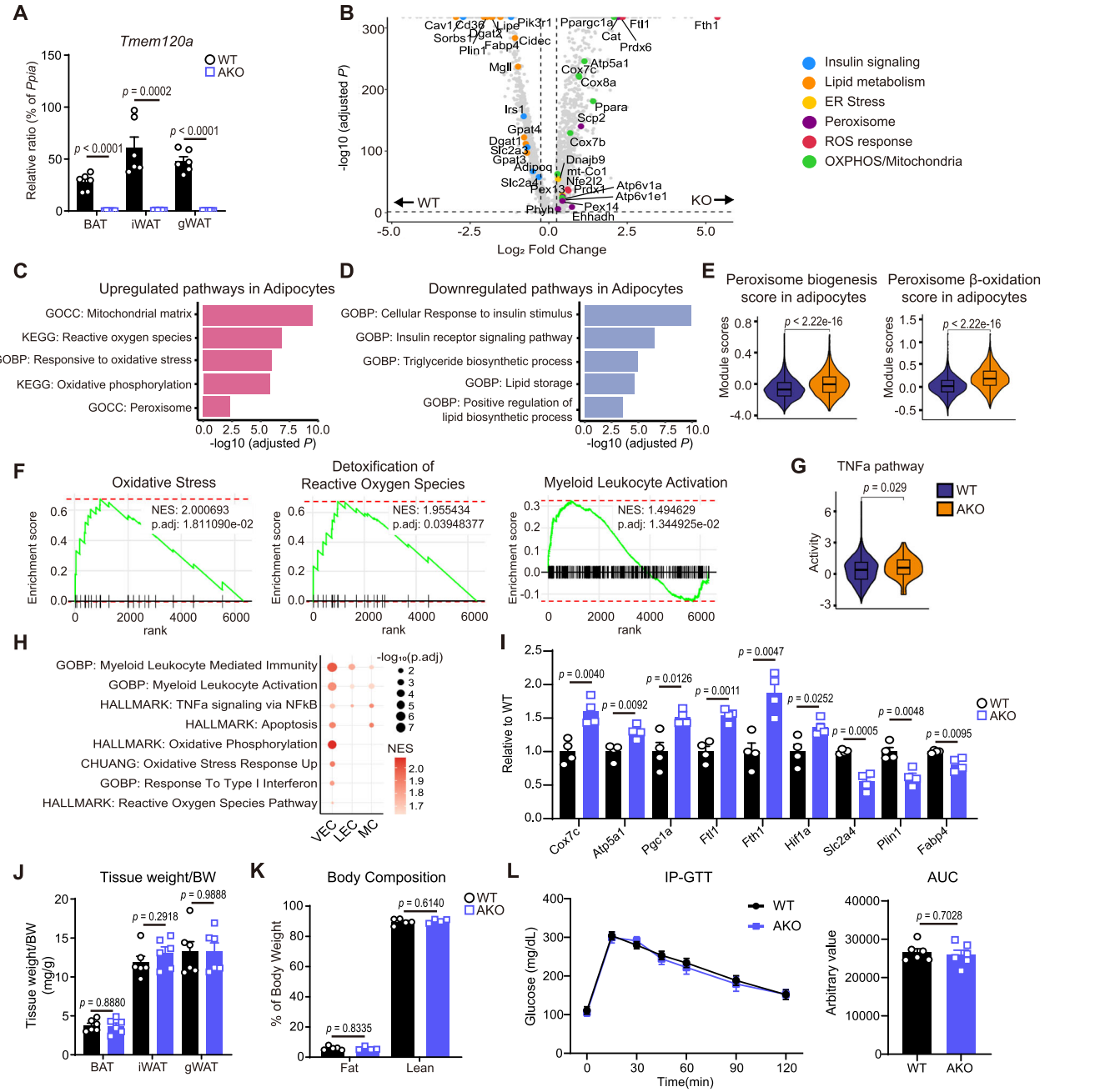

Fig. 6 | Single nucleus RNAseq reveals upregulation of genes involved in oxidative stress and inflammation by TMEM120A KO in adipocytes. A mRNA levels of *Tmem120a* in adipose tissues of WT and TMEM120A AKO mice. $n = 6$. **B** Volcano plot of differentially expressed genes (DEGs) in adipocytes between TMEM120A AKO and WT mice. Male mice at 20 weeks of age were used for this experiment. Dashed lines indicate an adjusted p value = 0.05 and $|\log_2$ fold change$|$ = 0.25. Genes (dots) are colored by associated pathways. **C**, **D** Selected upregulated and downregulated pathways in adipocytes of TMEM120A AKO mice compared to WT. **E** Violin plots showing peroxisome biogenesis and β-oxidation scores in adipocytes across conditions (WT, $n = 7{,}264$; AKO, $n = 2{,}127$ nuclei). **F** Enrichment plots for three representative pathways upregulated in macrophages of TMEM120A AKO mice compared to WT. Each plot shows the enrichment score (green line), the positions of genes in the ranked list (black ticks), and the maximum enrichment score (horizontal red dashed line). Normalized enrichment score (NES) and adjusted p value (p.adj) are indicated in each panel. **G** Violin plot showing pathway activity scores in macrophages across conditions (WT, $n = 868$; AKO, $n = 69$ nuclei). **H** Dot plot showing pathways enriched in TMEM120A AKO compared to WT mice for each cell type. The size of each dot represents the adjusted p value (p.adj), and the color indicates the NES. Only pathways with adjusted p value < 0.05 are shown. **I** mRNA levels of genes involved in oxidative phosphorylation, reactive oxygen species, lipid metabolism, and insulin sensitivity. $n = 4$. **J** Tissue weights of WT and TMEM120A AKO mice. $n = 6$. **K** Body composition analysis of WT and TMEM120A AKO mice. WT: $n = 5$; AKO: $n = 4$. **L** Intraperitoneal-glucose tolerance test (IP- GTT) of WT and TMEM120A AKO mice. $n = 6$. Data are presented as mean values ± SEM. Each point represents a biological replicate. p values were determined by an unpaired two-sided Student's t-test (**A**, **E**, **G**, **I**–**L**).

remodeling and to determine whether the observed transcriptional alterations are associated with phenotypic outcomes under metabolic stress conditions. We monitored the body weights weekly during the 12 weeks of feeding period and observed significantly increased body weight in TMEM120A AKO mice compared to WT after 3 weeks of HFD feeding (Fig. 7B and Supplementary Fig. 14A). Consistent with this trend, the weights of iWAT and gWAT were significantly increased while the weight of BAT remained unchanged in TMEM120A AKO mice

https://doi.org/10.1038/s41467-025-67870-7

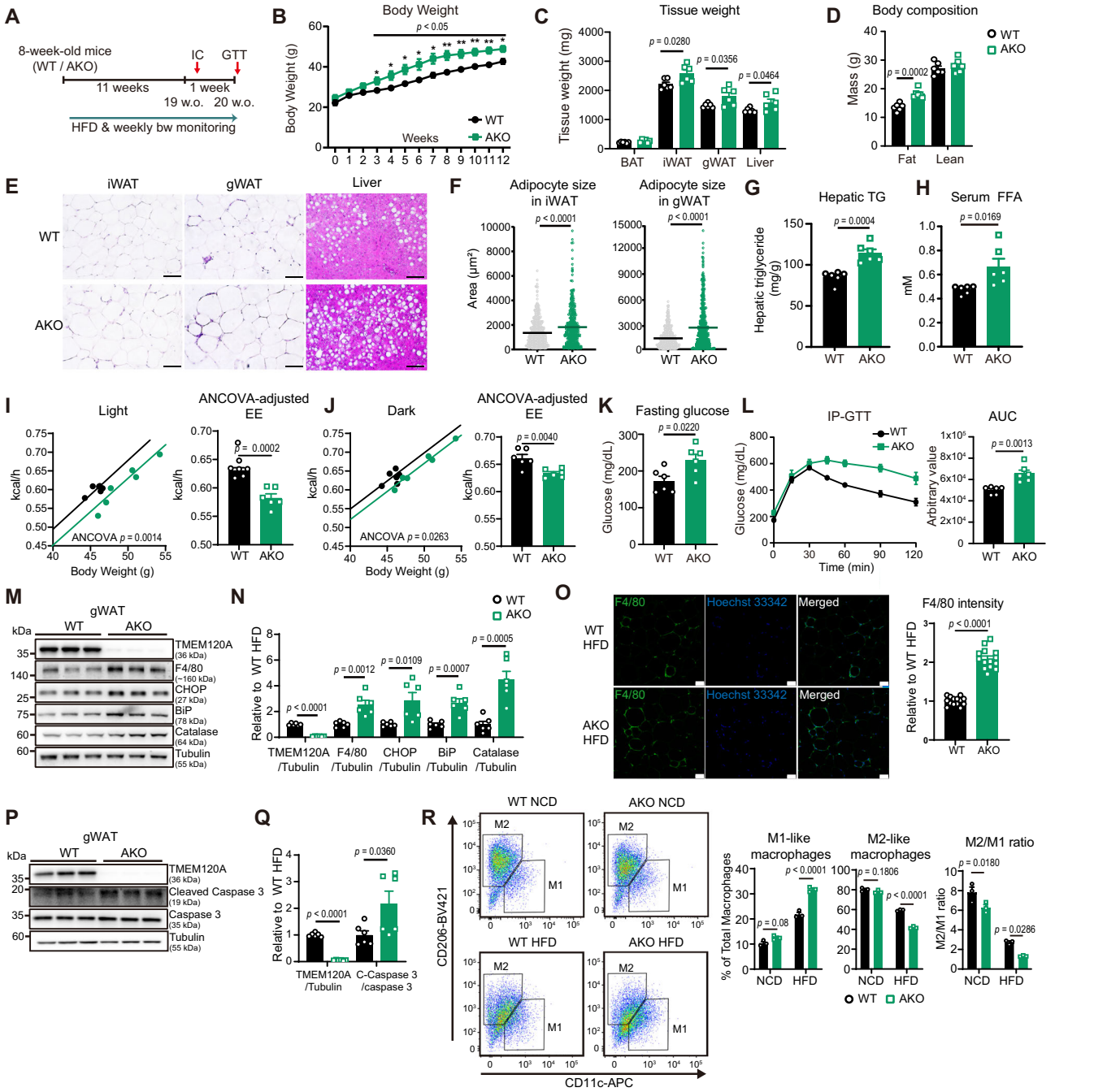

Fig. 7 | Adipocyte-specific deletion of TMEM120A exacerbates metabolic dysfunction in a diet–induced obesity mouse model. A Experimental design of WT and TMEM120A AKO mice, initiated at 8 weeks of age and subjected to a HFD for 12 weeks. Indirect calorimetry was conducted during week 12, and glucose tolerance test (GTT) was performed after 12 weeks of HFD feeding. **B** Body weight monitoring of WT and TMEM120A AKO mice. $n = 6$. **C** Tissue weights of adipose tissue depots and the liver of WT and TMEM120A AKO mice. $n = 6$. **D** Body composition of WT and TMEM120A AKO mice. $n = 6$. **E** Representative H&E staining of iWAT, gWAT, and liver. Scale bar = 50 μm. **F** Area of adipocytes in iWAT and gWAT from WT and TMEM120A AKO mice. The number of adipocytes measured for WT and TMEM120A AKO are 500. Hepatic TG (**G**) and serum FFA (**H**) levels of WT and TMEM120A AKO mice. $n = 6$. **I**, **J** Regression plots of energy expenditure against body mass (ANCOVA using body mass as a covariate, two-sided without adjustment, $n = 6$) and ANCOVA-adjusted energy expenditure (predicted energy expenditure at the mean body mass 47.63 g). Fasting glucose levels (**K**) and intraperitoneal- (IP-) GTT (**L**) of WT and TMEM120A AKO mice. $n = 6$. **M**, **N** Immunoblot of ER stress and inflammation markers in gWAT of WT and TMEM120A AKO mice fed a HFD for 12 weeks. $n = 6$. **O**. Immunofluorescence staining of F4/80 in gWAT of WT and TMEM20A AKO mice and quantification of F4/80 fluorescence intensity. $n = 14$. Scale bar = 50 μm. Each point represents a technical replicate. **P**, **Q** Immunoblot analysis of apoptosis marker in gWAT of WT and TMEM120A AKO mice. $n = 6$. **R** Flow cytometric analysis of $CD45^+CD11b^+CD11c^+$ (M1-like) and $CD45^+CD11b^+CD206^+$ (M2-like) macrophages in SVFs isolated from gWAT of WT and TMEM120A AKO mice. $n = 3$. Data are presented as mean values ± SEM. Each point represents a biological replicate except (**O**). p values were determined by an unpaired two-sided Student's t-test (**B**–**D**, **F**–**H**, **K**, **L**, **N**, **O**, and **Q**) and a two-way ANOVA followed Sidak's multiple comparisons test (**R**).

fed HFD for 12 weeks (Fig. 7C). Supporting these findings, fat mass increased in TMEM120A AKO mice subjected to 12 weeks of HFD feeding (Fig. 7D) and histological analysis confirmed larger adipocytes in iWAT and gWAT of TMEM120A AKO mice fed HFD for 12 weeks (Fig. 7E, F). Additionally, TMEM120A AKO showed elevated circulating FFAs and increased hepatic TG content, consistent with ectopic fat deposition in the liver (Fig. 7G, H). To determine whether the observed changes in body and tissue weight resulted from impaired energy metabolism, we performed indirect calorimetric analysis. Relative to WT, body mass–adjusted energy expenditure was significantly lower in TMEM120A AKO mice during both the light and dark phases, as assessed by ANCOVA with body mass as a covariate (Fig. 7I-J and Supplementary Fig. 14D-G).

Next, we assessed the impact of TMEM120A AKO on glucose homeostasis. TMEM120A AKO mice exhibited elevated fasting glucose levels and glucose intolerance (Fig. 7K, L and Supplementary Fig. 14B, C). Moreover, protein and mRNA levels of ER stress markers, inflammatory mediators, and adipocyte death-related genes were increased in iWAT and gWAT of TMEM120A AKO mice fed a HFD (Fig. 7M-Q, Supplementary Fig. 15A-B, and Supplementary Fig. 16A-D). Consistent with an inflammatory shift, TMEM120A AKO mice showed increased proportions of M1-like macrophages and reduced proportions of M2-like macrophage in gWAT under HFD (Figure s). Interestingly, peroxisomal β-oxidation markers (*Acaa1a, Abcd3, Acox1*, and *Hsd17b4*) and peroxisome biogenesis genes (*Pex3, Pex5, Pex7, Pex16* and *Pex19*) were upregulated in gWAT of HFD-fed TMEM120A AKO mice, accompanied by increased catalase protein abundance (Fig. 7M and Supplementary Fig. 16C). However, UCP1 expression in iWAT was comparable between WT and AKO mice, and UCP1 was undetectable in gWAT of either genotype under HFD condition (Supplementary Fig. 15A-B). These findings suggest that impaired lipid cycling in TMEM120A-deficient adipocytes results in lipid accumulation, subsequently inducing ER stress and triggering peroxisome biogenesis and peroxisomal β-oxidation to mitigate excess lipid accumulation in adipocytes.

Discussion

In this study, we identify TMEM120A as an ER-resident CoA-binding scaffold that orchestrates LC-acyl-CoA flux to drive FA re-esterification in adipocytes. TMEM120A is highly enriched in white adipocytes yet markedly suppressed in both diet-induced mouse obesity models and human obesity. In vitro gain- and loss-of-function studies reveal that TMEM120A increased ER-CoA availability and enhances re-esterification during lipolysis. Mechanistically, TMEM120A preserves ER CoA availability, thereby sustaining CoA-dependent interactions with ACSL1 and ACSL3. This interaction facilitates the conversion of FFAs into LC-acyl-CoAs by ACSL1 and ACSL3, subsequently promoting their re-esterification into TGs. In vivo adipocyte-specific *Tmem120a* knockout impairs lipolytic flux and activation of the TG/FA futile cycle, reducing ATP-consuming lipid turnover and thereby lowering energy expenditure in response to acute β-adrenergic stimulation. In HFD-induced obesity, adipocyte-specific TMEM120A deletion triggers BiP/CHOP-mediated ER stress, promotes lipotoxic ROS accumulation, leads to reduced oxygen consumption, hepatic steatosis, and glucose intolerance. These findings establish TMEM120A as a critical regulator of ER CoA dynamics and lipid cycling and adipose tissue homeostasis.

TMEM120A was initially identified as NET29, a nuclear envelope transmembrane protein enriched in the inner nuclear membrane of liver and fibroblast cells[36]. Early studies suggested roles for TMEM120A in nuclear architecture, adipocyte differentiation, and chromatin organization[22,35,37]. More recent reports have implicated TMEM120A in non-adipocyte contexts, such as mechanosensation in dorsal root ganglion neurons[23] and modulation of antiviral signaling via STING activation[38]. However, some of these functional interpretations, such as TMEM120A acting as an ion channel, have been challenged by structural and electrophysiological analyses[19–21]. Our findings clarify this ambiguity by demonstrating that in adipocytes, TMEM120A is localized to the ER rather than the nuclear envelope, where it functions not as an ion channel or fatty acid elongase, but as a CoA-binding protein that facilitates lipid metabolic flux. These observations highlight the importance of context-dependent functions of TMEM120A and underscores the need to study its role within relevant metabolic tissues.

A key finding of our study is that a conserved CoA-binding pocket, validated by W193A mutagenesis, confers the ability to retain and recycle free CoA within the ER. Notably, multi-species alignment shows 100% conservation of W193, and substituting alanine disrupts pocket integrity and significantly weakens CoA binding affinity (WT: $K_d = 0.69 \pm 0.05$ μM; W193A: $K_d = 198.41 \pm 0.81$ μM)[20], underscoring W193's essential role in maintaining the structural integrity of the CoA-binding pocket. In the ER, CoA released during TG and phospholipid biosynthesis is thought to be rapidly recycled to sustain LC-acyl-CoA formation. Despite the central role of CoA in lipid metabolism, the identity of ER CoA transporters or recycling systems remains unknown. Efficient CoA handling, however, is considered essential for sustaining lipid synthesis and remodeling. Mitochondria, for example, require robust CoA availability for the tricarboxylic acid cycle, β-oxidation, and other metabolic processes[39]. In addition, CoA regulates acyl-CoA turnover by inhibiting acyl-CoA thioesterases (ACOTs), preventing excessive hydrolysis of acyl-CoAs when CoA levels are sufficient[40]. This dual role-both as a cofactor and feedback regulator-underscores the importance of CoA homeostasis in cellular metabolism. By analogy, maintaining a sufficient CoA pool in the ER is likely vital for driving lipid anabolic pathways.

Our data underscore the principle that organelle-specific acyl-CoA pools dictate metabolic fate, with TMEM120A physically interacting with ACSL1 and ACSL3 at the ER to direct FA flux towards anabolic re-esterification. Canonically, LC-acyl-CoAs are partitioned between mitochondrial or peroxisomal β-oxidation and ER-based lipogenesis or membrane remodeling[41,42]. ACSL1, the predominant acyl-CoA synthetase isoform in adipose tissue, is well-established in directing FAs toward mitochondrial β-oxidation[15,26]. Although adipocyte-specific deletion of ACSL1 displayed normal FA re-esterification in vivo[15], ACSL1 predominantly localizes to the ER in adipose tissues, and in vitro studies have suggested its involvement in re-esterification in adipocytes[43,44]. In contrast, ACSL3 is a well-characterized isoform localized to both LDs and the ER, primarily mediating re-esterification across various cell types[27,29]. Notably, while ACSL3 is detectable on LDs, quantitative analyses indicate that approximately 68% of ACSL3 remains ER-associated following FA stimulation[27]. We found that TMEM120A enhances ER localization of ACSL3, further amplifying TG synthesis.

In line with this view, BioID proteomics in hepatocytes revealed that ACSL1 forms discrete complexes with β-oxidation enzymes (CPT1A, HADHB) on the outer-mitochondrial membrane and with lipogenic enzymes (DGAT2, GPAT1) on the ER/mitochondria associated membranes. These interactions are dynamically regulated by hormonal cues such as glucagon and insulin[45]. These data support the idea that protein-scaffolded 'micro-domains' dictate metabolic fate of nascent acyl-CoAs—whether routed toward oxidation or re-esterification, paralleling the TMEM120A-ACSL interface described here in adipocytes. Such compartmentalized pools of acyl-CoAs also influence downstream redox signaling, ROS production, and lipid-peroxidation susceptibility[30]. Clinically, disruptions in acyl-CoA compartmentalization are linked to metabolic dysfunction, as exemplified by impaired peroxisomal acyl-CoA turnover driving insulin resistance and autophagy-dependent muscle wasting[46]. By stabilizing the TMEM120A-ACSL interaction at the ER, TMEM120A may serve as a metabolic gatekeeper that promotes lipid turnover while mitigating organelle stress and redox imbalance, offering a strategic node for therapeutic intervention.

Beyond its role in anabolic pathways, TMEM120A also governs catabolic lipid dynamics: by reducing levels of LC-acyl-CoA that inhibit cAMP generation and lipolysis, TMEM120A potentiates cAMP-PKA signaling, increase net lipolysis and futile cycling to enhance energy expenditure. Our findings demonstrate that TMEM120A sustains TG/FA cycling to alleviate lipolysis-induced ER stress and lipotoxicity, thereby maintaining adipocyte homeostasis. Conversely, TMEM120A loss promotes inflammation, insulin resistance, and reduced energy expenditure under HFD feeding. Of note, we repeated the indirect calorimetry experiment to strengthen confidence in our observations. Although the repeated cohort showed inter-cohort variability in metabolic readouts, both cohorts (Fig. 7I, J and Supplementary Fig. 14) displayed consistent results, demonstrating that TMEM120A AKO significantly reduces energy expenditure. These results identify TMEM120A as a key regulator of adipose remodeling during metabolic stress and suggest that restoring its function may represent a therapeutic strategy against obesity-associated dysfunction. Consistent with prior studies, TMEM120A-mediated partial re-esterification of FAs buffers toxic lipid intermediates and facilitates rapid adaptation to energy demands[31,47].

Futile lipid cycling has emerged as a promising therapeutic target to increase energy expenditure independently of UCP1-mediated thermogenesis[10,48,49]. For example, chronic β3-adrenergic stimulation augments TG/FA cycle in WAT[11], improving glucose tolerance even in aged or UCP1-deficient mice[50]. Similarly, prolonged FGF21 administration elevates futile lipid cycling in WAT, increases whole-body energy expenditure, and drives weight loss without canonical uncoupling mechanisms[49]. Our study builds on this growing body of evidence by uncovering a mechanistic link between ER CoA availability, acyl-CoA synthesis, and re-esterification capacity.

In conclusion, our study identifies TMEM120A as an ER-localized CoA-binding protein that coordinates intracellular CoA dynamics, promotes FA re-esterification, and maintains lipid homeostasis in adipocytes. While future studies employing high-resolution structural and biochemical approaches will be required to capture the dynamics of TMEM120A–CoA binding and the molecular mechanism of CoA transfer, our findings uncover a previously unrecognized mechanism linking ER CoA handling to lipid cycling. By addressing a critical gap in how CoA availability is controlled within the ER, this work provides insight into the spatial regulation of lipid flux and established a foundation for therapeutic strategies targeting adipose tissue in metabolic disease.

Methods

Ethics statement

All experimental procedures involving animals were approved by the Institutional Animal Care and Use Committee of Seoul National University (SNU-1905093-3, SNU-230418-2-2) and complied with the guidelines of the Ministry of Food and Drug Safety for the ethical use of laboratory animals. Human subject research was conducted in accordance with the Declaration of Helsinki. Written informed consent was obtained from all participants, and the study was approved by the Institutional Review Board of Korea University Guro Hospital (IRB No. 2022GR0095).

Chemical reagents

The ABHD5 ligand SR-3420 (1-(3-(3,5-bis(trifluoromethyl)phenyl)propyl)−3-(10-methyl-11-oxo-10,11-dihydrodibenzo[b,f][1,4] thiazepin-8-yl)urea) was provided by J.G.G[34].

Human samples

This study was conducted in accordance with the Declaration of Helsinki and was approved by the Institutional Review Board of Korea University Guro Hospital (IRB No. 2022GR0095). All participants provided individual written informed consent before their samples were collected, permitting the anonymized use of their clinical information for research. A total of 24 individuals (15 men and 9 women), aged between 9 and 79 years, were included. Subcutaneous adipose tissue specimens were collected, rapidly frozen, and stored at −80 °C until analysis. Recruitment was open to both sexes without intentional gender-based selection. Participant sex was identified based on self-reported information. Detailed demographic and tissue characteristics for all human samples are summarized in Supplementary Table 1.

Animal studies

Mice were maintained under controlled conditions (22 ± 1 °C, 50% ± 5 humidity, 12 h light/12 h dark cycle) with ad libitum access to food and water in Animal Center for Pharmaceutical Research at Seoul National University. C57BL/6N-*Tmem120a*^{tm1Cyagen} (*Tmem120a*$^{flox/flox}$) mice were purchased from Cyagen and bred with C57BL/6J-Adipoq-Cre (B6;FVB-Tg(Adipoq-cre)1Evdr/J: stock#028020) mice to generate the following genotypes: *Tmem120a*$^{flox/flox}$ without Adipoq-Cre (WT), *Tmem120a*$^{flox/flox}$; Adipoq-Cre (TMEM120A AKO). Both WT and TMEM120A AKO mice share a mixed C57BL/6 N and C57BL/6 J genetic background. Male WT and TMEM120A AKO aged 8-20 weeks were used for experiments. For diet-induced obesity, mice aged 8 weeks were fed with a high-fat diet (HFD) (60% fat, Research Diets, cat#D12492) for 12 weeks. Control mice were fed with a standardized rodent pellet diet (NCD) (Purina, cat#38057) (Supplementary Table 4). CL316,243 (CL) (Tocris, 1 mg/kg mouse) was administered intraperitoneally to stimulate lipolysis in 8-week-old mice. Energy expenditure was measured by indirect calorimetry (PhenoMaster, TSE Systems, Germany). ANCOVA of energy expenditure was performed using the NIDDK Mouse Metabolic Phenotyping Centers (MMPC) online Energy Expenditure Analysis tool (http://www.mmpc.org/shared/regression.aspx). Body composition was estimated by nuclear magnetic resonance (NMR) scanning EchoMRI-700 (Echo Medical Systems). GTT and indirect calorimetry were conducted in separate cohorts of mice. Because GTT involves overnight fasting, glucose administration and repeated blood sampling, all of which influence metabolic parameters and impose additional stress on the mice. To avoid these confounding effects and ensure reliable measurements, we performed GTT and indirect calorimetry in independent cohorts.

Cell culture and differentiation

HEK293T cells from American Type Culture Collection (ATCC, CRL-3216) were cultured in Dulbecco's Modified Eagle Medium (DMEM) (Welgene, cat#LM001-07) supplemented with 10% fetal bovine serum (FBS) (Gibco, cat#16000044) and 1% penicillin/streptomycin (P/S, Welgene, cat#LS202-02). C3H10T1/2 (ATCC, CCL-226) cells were used to conduct in vitro adipocytes experiments and cultured in DMEM supplemented with 10% FBS and 1% P/S at 37 °C in a humidified atmosphere with 5% CO_2. For adipogenic differentiation, confluent C3H10T1/2 cells were treated with bone morphogenetic protein 4 (BMP4) (20 ng/mL, R&D systems, cat#314-BP-050) for 2 days, followed by a 3-day induction in differentiation medium containing isobutylmethylxanthine (0.5 mM, Sigma, cat#I5879-1G), dexamethasone (Cayman, 1 µM, cat#11015), insulin (10 µg/mL, Sigma, cat#I9278), indomethacin (0.125 mM, Cayman, cat#70270) and triiodothyronine (T3) (1 nM, Cayman, cat#16028). Cells were maintained for 3 additional days in medium containing insulin (1 µg/mL) and T3 (1 nM).

To stimulate lipolysis, fully differentiated C3H10T1/2 adipocytes were treated with either vehicle controls, isoproterenol (10 µM, Sigma, cat#I5627-5G), or SR-3420 (20 µM) for the indicated time points. To assess ER stress, C3H10T1/2 adipocytes were pre-treated with DGAT1 inhibitor A922500 (5 µM) for 1 h, followed by stimulation with isoproterenol (10 µM) for 3 h.

To induce TMEM120A overexpression, C3H10T1/2 adipocytes were treated with doxycycline (2 µg/mL, Sigma, D9891-5G) for 48 h.

DNA constructs and stable cell line generation

Mouse *Tmem120a* (NM_172541) ORF Clone was purchased from Origene. To generate doxycycline-inducible cell line, C-terminus Myc-tagged *Tmem120a* ORF clone or C-terminus GFP-tagged *Tmem120a* ORF clone were inserted to the lentiviral transfer vector pCW57.1 (Addgene, cat#41393) using NheI-HF and SalI-HF. Lentiviral particles were produced by co-transfecting with pCW57.1 constructs, psPAX2 (Addgene, cat#12260), and pMD2.G (Addgene, cat#12259) in 4:3:1 ratio using jetPRIME transfection reagent (Polyplus, cat#114-15). Viral supernatants were collected, filtered (0.45 µm), and used to transduce C3H10T1/2 cells were in the presence of polybrene (8 µg/mL, Santa Cruz, cat#sc-134220) for 48 h. Cells were selected with puromycin (2 µg/mL, Sigma, cat#P8833).

To establish a stable *Tmem120a* KD cell line, complementary oligonucleotides targeting the coding sequence of *Tmem120a* were purchased from the Sigma MISSION shRNA clone (TRCN0000247877: forward oligo (5′- CCGGCAAAGACGAGTACGAGAAATTCTCGAGAATT TCTCGTACTCGTCTTTGTTTTTG −3′) and reverse oligo (5′- AATTC AAAAACAAAGACGAGTACGAGAAATTCTCGAGAATTTCTCGTACTCG TCTTTG). The oligos were annealed via thermal cycling and ligated into pLKO.1 TRC-cloning vector (Addgene, cat#10878) following digestion with AgeI-HF and EcoRI. Lentiviral particles were subsequently generated and used to transduce C3H10T1/2 cells as describe above.

pCMV NucleoBAS-ABHD5^{R229N}-PLIN5$^{384-417}$ and pINDUCER20-NucleoBAS-ABHD5^{R299N}-PLIN5$^{384-417}$ were provided from E.M[33].

The C3H10T1/2 cell line stably expressing a doxycycline-inducible LC-acyl-CoA FRET sensor (pCFP-ABHD5^{R299N}-YFP-PLIN5$^{384-417}$) was generated by transducing cells for 24 h with pINDUCER20-based lentivirus encoding the construct, followed by selection with G418 selection (1 mg/mL, Gibco, cat#10131035) for 7 days.

Compartment-specific protein–protein interactions were assessed using the BiFC assay, with VN173 fused to TMEM120A in both C- and N-terminal orientations. For N-terminal fusion of VN173, the stop codon (TAG) in pBiFC-VN173 (Addgene #22010) was replaced with GGT (glycine), and the mouse *Tmem120a* ORF clone was inserted through a single BamHI restriction site. For C-terminal fusion of VN173, the mouse *Tmem120a* ORF clone was ligated into pBiFC-VN173 following double digestion with HindIII and SalI. The mouse *Acsl3* (NM_028817) ORF clone was subcloned into pBiFC-VC155 (Addgene #22011) following double digestion with SalI and XhoI. Each construct (250 ng) was transfected into HEK293T cells for 24 h.

Site-directed mutagenesis

To generate mutant *Tmem120a* sequence, EZchange Site-directed Mutagenesis kit (Enzynomics, cat#EZ004S) was used following the manufacturer's manual. nPfu-Forte DNA polymerase, mouse *Tmem120a* ORF Clone, and the indicated primers (W193A forward: 5′-CGG TTT TCC ATC ATT ATG TGT CC −3′, W193A reverse: 5′- CCC AGC CTT TGA TCC TGG A −3′) were amplified to generate the potential active site mutant sequences. As a result, Trp 193 was substituted by Ala 193 in W193A mutation. Resulting constructs were verified by DNA sequencing and cloned into pCW57.1 for stable expression as described above.

Magnetic cell sorting

Stromal vascular fraction (SVF) cells were labeled with anti-F4/80-FITC (1:50, Biolegend, cat#123108) for 1 h at 4 °C followed by incubation with anti-FITC-microbeads (1:10, Miltenyi Biotec, cat#130-048-701) incubation for 30 min at 4 °C. Magnetic separation was performed to isolate F4/80$^+$ cells. The remaining F4/80$^-$ cells were subjected to PDGFRα selection using a PDGFRα MicroBead kit (Miltenyi Biotec, cat#130-101-502).

Flow cytometry

gWATs were finely minced and digested with collagenase type I (Gibco, cat# 17100-017) in Krebs-Ringer bicarbonate buffer (KRBB) containing 1% bovine serum albumin (BSA) at 37 °C. Following digestion, red blood cells (RBCs) were removed using RBC lysis buffer, and the resulting SVF was washed twice with KRBB containing 1% BSA. SVF cells were incubated with fluorescence-conjugated primary antibodies or isotype-matched control IgG for 90 min at 4 °C. To identify macrophage populations, leukocytes were first gated as CD45$^+$ using anti-CD45 (Invitrogen, clone 30-F11, cat#11-0451-82) and macrophages were identified as CD11b$^+$ cells anti-CD11b (BioLegend, clone M1/70, cat#101206) antibodies. M1-like and M2-like macrophages were subsequently distinguished by staining with anti-CD11c (BioLegend, clone N418, cat#117310) and anti-CD206 (BioLegend, clone C068C2, cat#141717) antibodies, respectively. Unstained and single-stained samples were used for fluorescence compensation. Flow cytometric analyses were performed using an LSRFortessa X-20 flow cytometer (BD Biosciences). Data acquisition was carried out with BD FACSDiva software (version 8.0) and further analyzed using FlowJo software (version 10.5.3; Tree Star). The gating strategy used for analysis is shown in Supplementary Fig. 17.

Quantification of intracellular cAMP levels

Intracellular cAMP levels were measured using a direct competitive ELISA (Enzo, cat#ADI-900-066). Briefly, C3H10T1/2 adipocytes were lysed with 0.1 M HCl for 10 min and centrifuged. Samples and acetylated standards were added to antibody-coated wells and incubated with a cAMP-alkaline phosphatase conjugate and anti-cAMP antibody. After a 2 h incubation at room temperature with shaking, plates were washed and developed using p-nitrophenyl phosphate substrate for 1 h followed by addition of a solution of trisodium phosphate in water. Absorbance at 405 nm was recorded, and cAMP concentrations were calculated from a standard curve using AssayFitPro (v1.31), with normalization to protein content determined by BCA assay (Thermo Fisher, cat#23225).

Measurement of liver triglyceride content

To determine hepatic TG content, approximately 100 mg of liver tissue was incubated overnight at 55 °C in an ethanolic KOH solution (EtOH: 30% KOH = 2:1). Following digestion, the sample volume was adjusted to 1000 µL with 50% ethanol, vortexed, and centrifuged at 100 × *g* for 5 min. The supernatant was transferred to a fresh tube and diluted to a final volume of 1200 µL using additional 50% ethanol. From this solution, 200 µL was mixed with 215 µL of 1 M $MgCl_2$, incubated on ice for 10 min, and centrifuged again at 100 × *g* for 5 min. The final supernatant was used for TG measurement by reacting with glycerol reagent (Sigma, cat#F6428), as instructed by the manufacturer. TG concentration was calculated using a triolein standard curve.

Glucose tolerance test (GTT)

For glucose tolerance assessments, mice were fasted for 12 h prior to glucose administration. For the intraperitoneal glucose tolerance test (IP-GTT), D-(+)-glucose (2 g/kg body weight; Sigma, cat#49139) was administered via intraperitoneal injection, whereas for the oral glucose tolerance test (O-GTT), D-(+)-glucose (2 g/kg lean mass) was delivered by oral gavage. Blood glucose concentrations were recorded at designated time points using the Gluco Doctor Top glucometer (Allmedicus, cat#AGM-4100) and compatible test strips.

Immunoprecipitation

C3H10T1/2 adipocytes were lysed in lysis buffer (50 mM Tris-HCl (pH 7.4), 150 mM NaCl, 1 mM EGTA, 1 mM EDTA, 1% Triton X-100). A total of 1 mg of lysates was incubated with anti-c-Myc agarose (Thermo, cat#20168) overnight at 4 °C on rotating shakers. Beads were rinsed

three times with TBS with 0.05% Tween-20 and eluted with c-Myc-Peptide (0.5 mg/mL, Thermo, cat#26184).

Subcellular fractionation

C3H10T1/2 adipocytes were harvested in isolation buffer (IB; 225 mM mannitol, 75 mM sucrose, 0.1 mM EGTA, 30 mM Tris-HCl, pH 7.4) supplemented with protease and phosphatase inhibitors. Adipocytes were homogenized using a syringe. Nuclei were pelleted at 600 x g, washed three times, and lysed in RIPA buffer. The supernatant (containing mitochondria and microsomes) was collected, and crude mitochondria were isolated at 10,000 × *g*, washed three times, and resuspended in mitochondria resuspending buffer (MRB; 250 mM mannitol, 5 mM HEPES, 0.5 mM EGTA, pH 7.4) supplemented with protease and phosphatase inhibitors. The remaining supernatant (cytosolic fraction containing microsomes) was collected, and microsomal fractions were obtained by ultracentrifugation at 100,000 x g and resuspended in MRB. 3 μg of protein was loaded per lane.

Quantitative PCR and western blot analysis

Total RNA was isolated from adipose tissue using TRIzol reagent, and cDNA was synthesized using the High-Capacity cDNA Reverse Transcription Kit (Applied Biosystems, cat#4368814). Quantitative PCR was conducted using iQ SYBR Green Supermix (Bio-Rad, cat#170-8884) on a CFX Connect Real-Time PCR Detection System (Bio-Rad). Relative transcript levels were calculated using the 2-ΔCt method with Peptidylprolyl isomerase A *(Ppia)* as the reference gene. qPCR primers were designed using NCBI Primer-BLAST and synthesized by Bionics Korea. Primer sequences are listed in Supplementary Table 3.

For protein analysis, tissues including BAT, iWAT, and gWAT were homogenized using tacoPrep Bead Beater in PRO-PREP buffer (iNtRON Biotechnology, cat#17081) supplemented with SIGMAFAST protease inhibitors (Sigma, cat#S8820) and PhoSTOP phosphatase inhibitors (Roche, cat#4906845001). Cultured adipocytes were lysed in RIPA buffer (Thermo Fisher, cat#89900) with the same inhibitor cocktail. Protein concentration was determined via BCA assay, and absorbance was read at 562 nm using a MultiSkan GO plate reader (Thermo Fisher). Proteins were separated by SDS-PAGE, transferred to PVDF membranes, and probed with primary antibodies. Primary antibodies against TMEM120A (Cat# 68229-1-Ig, 1:1000), TMEM120B (Cat# 24539-1-AP, 1:1000), ACSL3 (Cat# 20710-1-AP, 1:1000) were purchased from Proteintech, Perilipin 1 (customized, 1:1000), COXIV (cat#4850S, 1:1000), phospho-HSL (Ser660, cat#45804S, 1:1000), HSL (cat#4107S, 1:1000), α/β-Tubulin (cat#2148, 1:1000), Lamin A/C (cat#2032, 1:1000), VDAC (cat#4866, 1:1000), PDI (cat#3501, 1:1000) F4/80 (cat#30325S, 1:1000), ACSL1 (cat#9189, 1:1000), BiP (cat#3177, 1:1000), CHOP (cat#2895, 1:1000) and Caspase 3 (cat#9662, 1:1000) were purchased from Cell Signaling Technology, MCAD (cat#sc-365030, 1:1000) and Catalase (cat#sc-271803) were purchased from Santa Cruz Biotechnology, Anti-P-Perilipin 1 (Ser522, cat#4856, 1:1000) was purchased from Vala Sciences, UCP1 was purchased from Alpha Diagnostics (cat#UCP11-A, 1:1000), Horseradish Peroxidase-conjugated Goat anti-Rabbit IgG (H + L) Secondary Antibody (cat#31460, 1:5000) were purchased from Invitrogen, Horseradish Peroxidase-conjugated Goat anti-mouse IgG, light chain specific Secondary Antibody (cat#115-035-174, 1:1000) was purchased from Jackson ImmunoResearch. Detection was performed using HRP-conjugated secondary antibodies and visualized on a Fusion Solo chemiluminescence system (Vilber Lourmat). Band intensities were quantified using ImageJ (NIH, version 1.52a).

Live-cell imaging and immunofluorescence microscopy

C3H10T1/2 adipocytes were differentiated in a confocal dish as described above and treated with doxycycline (2 μg/mL) to induce expression of the FRET sensor and TMEM120A for 48 h prior to imaging. Live cell FRET imaging for LC-acyl-CoAs in C3H10T1/2 adipocytes was performed in a live cell chamber on Leica TCS SP8 confocal microscope equipped with dual detectors and with continuous Adaptive Focus Control between each frame. Cerulean was excited at 405 nm, and emissions from ECFP and EYFP-FRET were collected at 450–515 nm and 520–600 nm, respectively. Images were captured every 30 s in laser scanning mode with bidirectional scanning and FRET efficiency was quantified as the EYFP-FRET/ECFP emission ratio using Leica Application Suite X 3.6.

To analyze subcellular localization of TMEM120A, cells were fixed in 4% paraformaldehyde for 20 min, permeabilized in 0.3% Triton X-100 for 15 min, and then incubated in blocking buffer (PBS containing 3% BSA) for 1 h at room temperature. Cells were incubated overnight with primary antibodies against organelle markers (Calnexin, Lamin A/C, PDI, or Citrate Synthase; 1:100). Thereafter, Goat anti-Rabbit IgG Alexa Fluor 594 (Invitrogen, 1:300, cat#A11012) or Donkey anti-Mouse IgG Alexa Fluor 594 (Invitrogen, 1:300, cat#A21203) was applied for 1 h at room temperature. Nuclei were counter-stained with DAPI. For live cell imaging, live C3H10T1/2 cells and adipocytes were incubated in Hanks' Balanced Salt solution (HBSS) containing MitoTracker Red (1 μM), ER-Tracker Red (1 μM), CellMask™ Deep Red (1 μg/ml) and HCS LipidTOX™ Deep Red Neutral Lipid Stain (1:2500, Invitrogen, cat#H34477) for 30 min at 37 °C and 5% CO_2. After removing the probe-containing, serum-free medium, cells were incubated in fresh probe-free medium and immediately imaged on a Zeiss LSM800 confocal microscope equipped with a live-cell chamber. Images were processed and analyzed using ZEN 3.0 (Blue edition) software. Colocalization was quantified using the Coloc2 plugin in ImageJ by calculating Pearson's correlation coefficient.

For BiFC assay, BiFC signals were detected using 488 nm excitation with emission collected at 510–570 nm. Images were acquired and analyzed using Leica Application Suite X.

Histology and immunohistochemistry

BAT, iWAT, and gWAT were dissected, fixed in 10% neutral-buffered formalin (Sigma, cat#HT50128) for 24 h at 4 °C, and subsequently embedded in paraffin. Sections of 5 μm thickness were prepared using a microtome. The sections were deparaffinized sequentially (2 × 10 min in xylene; 10 min in 50:50 xylene:ethanol; 5 min in 100% ethanol; 5 min in 95% ethanol; 5 min in 70% ethanol). Sections were rinsed in distilled water, subjected to antigen retrieval by boiling in citrate buffer (pH 6.0) for 10 min, and cooled to room temperature. For H&E staining, deparaffinized sections were stained with ClearView Staining Hematoxylin (BBC Biochemical, cat#MA010081) and Eosin Y Alcoholic solution (BBC Biochemical, cat#3610). The images were obtained with Nikon Elements (NIS BR Analysis ver 5.10.00). For immunofluorescence staining, sections were blocked with PBS containing 3% BSA, then incubated overnight at 4 °C with anti-F4/80 antibody (1:400) in 3% BSA in PBS. After three washes in PBS, slides were incubated for 1 h at room temperature with Alexa Fluor 488-conjugated goat anti-rabbit IgG (Invitrogen, 1:300, cat#A11008), counterstained with Hoechst 33342 (Thermo, cat#62249) and mounted in Permafluor Mountant (Thermo Fisher Scientific, cat#TA-030-FM). Confocal images were acquired on a Leica TCS SP8 confocal microscope and processed with Leica Application Suite X 3.6. Bright-field images were obtained on a Nikon Ts2-FL microscope and processed with NIS Elements BR Analysis (version 5.10.00). Adipocyte size in histological sections of iWAT and gWAT was quantified using Adiposoft software[51]. Only fully enclosed adipocytes within the field of view were included in the analysis. Individual adipocytes were manually delineated, and their cross-sectional areas were calculated accordingly.

ROS assay

Intracellular ROS levels were assessed using the H_2DCFDA fluorescent probe (Invitrogen, cat#D399). Cells were incubated with 10 μM H_2DCFDA in HBSS at 37 °C for 45 min in the dark. Following incubation,

cells were washed three times with PBS to eliminate residual dye. Fluorescence intensity was recorded at an excitation wavelength of 485 nm and emission at 530 nm using a SpectraMAX M5 microplate reader (Molecular Devices). Fluorescence values were normalized to total protein content as determined by BCA assay (Thermo Fisher Scientific, cat#23225).

Lipolysis assay (FFA & glycerol assay)

To evaluate lipolytic activity, free fatty acids (FFAs) and glycerol concentrations were measured in conditioned media or serum. FFA levels were determined using the NEFA-HR(2) assay kit (Wako Diagnostics, cat#438-91691, #438-91791, #438-91891, and 438-91991) and glycerol concentrations were quantified using the Free Glycerol Reagent (Sigma, cat#F6428). For the FFA assay, samples were incubated with reagent A for 3 min, followed by reagent B for 7 min, and absorbance was read at 546 nm. Glycerol detection involved a single 3 min incubation with reagent, and absorbance was measured at 540 nm.

Coenzyme A detection assay

Coenzyme A (CoA) levels were measured using the Coenzyme A Assay Kit (ab102504, Abcam). ER-enriched microsomal fractions were isolated by subcellular fractionation as described above. Briefly, the colorimetric assay was performed by diluting each microsomal fraction with Assay Buffer 5 at a 1:1 ratio. For CoA conversion, samples were incubated with 10 μl of ACS substrate and 2 μl of CoA Converter Mix at 37 °C for 30 min. To develop CoA-dependent signals, samples were then incubated with a reaction mix containing Assay Buffer, Acyl-CoA Enzyme Mix, and OxiRed™ probe at 37 °C for 30 min. Absorbance was measured at 570 nm to quantify CoA levels and normalized by protein concentrations.

CoASH extraction from isolated ER

To extract CoAs from the isolated ER fraction, 500 μL of 0.1% (v/v) formic acid in water was added to the sample, and the resulting suspension was subjected to three freeze–thaw cycles, alternating between liquid nitrogen and 4 °C, to ensure complete membrane lysis while minimizing CoA degradation during process. Subsequently, a liquid-liquid extraction (LLE) was performed to remove non-polar interferences by adding 500 μL of hexane. The biphasic mixture was vortexed for 30 s and centrifuged at 13,000 × g for 10 min at 4 °C. The upper organic (hexane) layer was carefully removed and discarded. This hexane extraction was repeated once. The final aqueous layer was collected, filtered through a 0.20 μm syringe filter, and evaporated to dryness under a gentle stream of nitrogen. The dried residue was then reconstituted in 100 μL of water prior to LC–MS/MS analysis.

Quantification of CoA using liquid chromatography–tandem mass spectrometry (LC-MS/MS)

5 μL of the extracted CoA diluent was analyzed using an Agilent 1290 UPLC system coupled with an Agilent 6495D triple quadrupole LC-MS/MS system, equipped with a Waters ACQUITY UPLC BEH C18 column (2.1 × 100 mm, 1.7 μm). LC separation was performed at a flow rate of 0.15 mL/min with the column temperature maintained at 40 °C, employing a gradient elution using mobile phase A (50 mM ammonium acetate in water) and mobile phase B (acetonitrile). The gradient was programmed as follows: 0–1 min at 1% B, ramping to 5% B by 1.1 min, increasing further to 25% B by 7 min, reaching 40% B at 8 min and holding until 3 min, returning to 1% B by 11.1 min, and equilibrating at 1% B until 17 min. CoA eluting from the column was ionized in positive electrospray ionization mode under the following conditions: dry gas flow rate at 13 L/min; dry gas temperature at 250 °C; nebulizer pressure set at 35 psi; sheath gas flow rate at 11 L/min; sheath gas temperature at 300 °C; capillary voltage at 3500 V; and nozzle voltage at 1500 V. CoA was detected in multiple reaction monitoring (MRM) mode, monitoring the transition from the precursor ion m/z 768.1 to the product ion m/z 261.0[52]. The targeted MRM data were processed using Agilent Mass Hunter Quantitative Analysis 10.0 and CoA concentrations were determined employing an external standard calibration curve. The example of standard fragmentation and lipid annotation are provided in Supplementary Fig. 18.

TUNEL assay

Apoptotic cells were detected using the TUNEL Assay Kit-HRP-DAB (ab206386, Abcam). Deparaffinized tissue sections were permeabilized by incubation with Proteinase K for 20 min at room temperature, followed by rinsing with TBS for 5 min. Endogenous peroxidase activity was quenched with 3% H_2O_2 in methanol, and sections were again rinsed with TBS for 5 min. For TdT-mediated labeling, sections were incubated with the TdT enzyme mix for 90 min, and the reaction was terminated with Stop Buffer for 5 min. After blocking with blocking buffer for 10 min, samples were incubated with the conjugate diluted 1:25 in blocking buffer for 30 min. Apoptotic signals were visualized by incubation with DAB solution for 15 min. Sections were rinsed in DDW for 5 min and counterstained with Methyl Green for 3 min. To reduce nonspecific background, slides were sequentially washed with 100% ethanol and 100% methanol (four times each), then mounted using an organic mounting medium. Images were acquired after overnight incubation. Apoptotic cells were visualized as dark brown signals, whereas non-apoptotic cells appeared blue-green.

FA elongation assay

HEK293T cells were transfected with either pCMV6-Tmem120a-Myc or an empty vector using jetPRIME transfection reagent. After 24 h, cells were incubated with DMEM containing 10% FBS for 24 h. The microsomal fractionation was performed, followed by the fatty acid elongation assay. Cells were washed and resuspended in 3 mL of ice-cold sucrose/HEPES and dounce-homogenized. The homogenate was centrifuged 1000 x *g* for 7 min at 4 °C. The pellet was resuspended in 1 mL of sucrose/HEPES, dounce-homogenized, and the suspension was centrifuged at 1000 x *g* for 7 min at 4 °C. The supernatants were combined and re-centrifuged at 2000 x *g* for 30 min at 4 °C. Supernatant from this centrifugation was centrifuged at 105,000 x *g* for 60 min at 4 °C. The resultant pellets were resuspended in 0.1 mL of 0.1 M Tris-HCl, pH 7.4. The assay mixtures (0.1 mL total, including protein addition) contained 100 μM Tris-HCl, pH 7.4, 200 μM palmitoyl-CoA, 500 μM NADPH, and 200 μg of freshly obtained microsomal protein. After 10 min of preincubation at 37 °C, the reaction was initiated by the addition of 60 μM ^{13}C-malonyl-CoA and carried out for 1 h at 37 °C. The incubation was terminated by addition of 0.1 mL of 5 M KOH in 10% methanol and saponified at 65 °C for 45 min. Then the samples were cooled and acidified with 0.1 mL of ice-cold 5 N HCl.

Upon the elongating reaction, FAs were extracted by methyl-tert-butyl ether (MTBE) with minor modifications[53]. Briefly, 300 μL of MeOH and 1 mL of MTBE were added to 300 μL of elongated products, the mixture was then shaken at 4 °C for 60 min before centrifuging at 16,000 x g for 10 min for phase separation. The upper lipid-containing organic phase was dried in a vacuum centrifuge. Extracted lipids were dissolved in 10 μL of chloroform/methanol (2:1) and diluted with 40 μL of acetonitrile /isopropyl alcohol/water (65:30:5).

For FAs measurement, liquid chromatography-mass spectrometry (LC-MS) analysis was conducted using the Waters Acquity UPLC system coupled with the Q Exactive Focus Orbitrap Mass Spectrometers (Thermo Fisher Scientific). Separation was achieved on a Kinetex C18 column (100 × 4.6 mm, 2.6 μm particle size; Phenomenex Cat# 00D-4462-E0). The mobile phase consisted of (A) 10 mM ammonium formate with 0.1% formic acid in acetonitrile/water (6:4), and (B) 10 mM ammonium formate with 0.1% formic acid in isopropyl alcohol/water (9:1). The gradient elution program was as follows: 0–3.25 min 15%-30% B, 3.25–4 min 30%-48% B, 4–16.75 min 48%-82% B, 16.75–17.5 min 82%-99% B, 18.25–18.4 min 99%-15% B, and 18.4–23 min

15% B. The total run time was 23 min, and the flow rate was 400 µL/min. Heated electrospray ionization (H-ESI) parameters were set as follows: 2.5 kV negative mode of capillary voltage, sheath gas 50 arbitrary units, auxiliary gas 15 arbitrary units, capillary temperature 320 °C, and auxiliary gas heater temperature 350 °C.

Incorporation of ^{13}C from ^{13}C-malonyl-CoA into fatty acids generates an M + 2 isotopologue, while endogenous unlabeled fatty acids are detected as M + 0. Thus, the appearance of M + 2 species directly reflects elongation activity. For C20:0, full scan mode was used, and extracted ion chromatograms were obtained for m/z 311.2956 (M + 0) and 313.3023 (M + 2). C20:3 was analyzed in selected-ion monitoring (SIM) mode, with the following m/z values monitored: 305.2486 for M + 0, 307.2553 for M + 2. Standard compounds used for fatty acids identification and constructing calibration curves include C18:3, C20:0, and C20:3 (Cayman #90230). The peak area of targeted fatty acids was extracted manually using Thermo Xcalibur 4.1 software and normalized to the total ion count of each sample for relative comparison.

Stable isotope tracing of FA re-esterification via ^{13}C-palmitate labeling

To prepare lipid-depleted FBS (dFBS), 10 g of fumed silica (Sigma, cat#S5130) was added per liter of serum. The mixture was incubated at room temperature for 1 h, followed by overnight mixing at 2–8 °C. The silica was removed by centrifugation at 2000 x g for 5 min, and the supernatant sterile-filtered (0.2 µm). The resulting dFBS was added to DMEM for subsequent cell culture. C3H10T1/2 adipocytes were treated with either vehicle or isoproterenol and 100 µM of ^{13}C-palmitate (Sigma, cat#292125) conjugated to 0.5% FA-free BSA was added to DMEM containing 10% dFBS for 2 h. For isotope negative control cells, 100 µM of palmitate (Sigma, cat#P5585) was treated for 2 h. After treatment, cells were washed twice—first with cold PBS and then with cold deionized water. Cells were scraped in 750 µL of cold deionized water and transferred to microcentrifuge tubes. An equal volume (750 µL) of ice-cold methanol was added to each tube. Samples were sealed and snap-frozen for subsequent analysis. Isotope tracing of FA re-esterification was performed using ^{13}C-palmitate conjugated to 0.5% FA-free BSA, enabling the detection of lipid incorporation with up to three ^{13}C-labeled lipids based on mass spectrometry. 2 h incubation with isotope-labeled palmitate, the extent of FA re-esterification into TG and PC was measured. Mass spectral ranges corresponding to isotopomers from M + 1 to M + 3 of lipids potentially containing palmitate (C16), including TG (e.g., TG 48:0) and PC (e.g., PC 34:1), were examined. These isotopomers, incorporating up to three ^{13}C derived from palmitate re-esterification (from M + 1 to M + 3 were verified to have no interfering signals originated from the detection of other lipid species or background noise at each retention time. The peak areas of all isotopomers, including both unlabeled (M + 0) and ^{13}C-labeled (M + 1, M + 2, M + 3) lipids, were determined from their extracted ion chromatograms and corrected using Isotope Distribution Calculator.

Lipid profiling

Lipid extraction from cells was performed using a modified freeze-thaw and biphasic extraction method[54]. Cells, stored at −80 °C until analysis, underwent three freeze-thaw cycles utilizing liquid nitrogen to achieve homogenization. After cell disruption, lipids were extracted via liquid-liquid extraction by adding 500 µL chloroform, vortexing for 30 s, and centrifuging at 13,000 x *g* for 3 min. The resulting non-polar (organic) layers were carefully transferred into separate microtubes, and the extraction was repeated once more. The combined organic layers were filtered through 0.20 µm PTFE syringe filters and dried under nitrogen evaporation. Dried lipids were reconstituted in 200 µL of isopropanol and further diluted by a factor of 1,000 prior to injection. Subsequently, 5 µL of the diluted lipid extracts were analyzed using an Agilent 1290 UPLC system coupled with an Agilent 6546 quadrupole time-of-flight high-resolution mass spectrometer, equipped with a Waters ACQUITY UPLC BEH C18 column (2.1 × 100 mm, 1.7 µm). LC separation was performed at a flow rate of 0.15 mL/min with the column temperature maintained at 40 °C, employing a gradient elution using mobile phase A (water:acetonitrile, 80:20 v/v, with 10 mM ammonium acetate and 0.1% formic acid) and mobile phase B (acetonitrile:isopropanol, 40:60 v/v, with 10 mM ammonium acetate and 0.1% formic acid). The gradient was programmed as follows: 0–3 min at 40% B, ramping to 85% B by 10 min, increasing further to 90% B by 13 min, reaching 100% B at 26 min and holding until 43 min, returning to 40% B by 45 min, and equilibrating at 40% B until 60 min. Lipids eluting from the column were ionized in positive electrospray ionization mode under the following conditions: dry gas flow rate at 8 L/min; dry gas temperature at 200 °C; nebulizer pressure set at 17 psi; sheath gas flow rate at 11 L/min; sheath gas temperature at 350 °C; capillary voltage at 3500 V; and nozzle voltage at 1000 V. Lipid species were identified based on retention time and isotopic pattern, and validated against an in-house library[55]. The untargeted full-scan data were analyzed using Agilent Mass Hunter Qualitative Analysis 10.0.

Total fatty acid profiling

Lipid extraction was performed from tissues using a modified version of the Matyash method[53]. A total of 300 µL of cold methanol containing the internal standard (nonadecanoic acid) was added directly to 20 mg of tissue, followed by 250 µL of cold water. Complete homogenization was achieved using a Precellys® Evolution homogenizer (Bertin Technologies, Montigny-le-Bretonneux, France) at 7,200 rpm for 30 seconds, repeated twice with brief cooling on ice between cycles. Subsequently, 1 mL of MTBE was added to the homogenate, and biphasic extraction was performed using a ThermoShaker (10 min, 1,500 rpm, 4 °C). After centrifugation (10 min, 16,000 x g), the upper organic phase was collected and dried under a gentle stream of nitrogen gas. Dried extracts were stored at −80 °C until analysis.

Total fatty acid profiling was conducted based on a modified version[56]. The dried lipid extract was reconstituted in 1 mL of 4:1 (v/v) methanol:12 M HCl and incubated at 100 °C for 1 h to allow methylation. The resulting fatty acid methyl esters (FAMEs) were extracted twice with 800 µL of hexane.

FAMEs were analyzed using an Agilent 7890B gas chromatograph (GC) coupled with a Pegasus BT time-of-flight mass spectrometer (ToF-MS; LECO Corporation, MI, USA). Chromatographic separation was achieved using a DB-5MS column (30 m × 0.25 mm, 0.25 µm; Agilent Technologies, DE, USA). The inlet temperature was set at 270 °C and the transfer line at 300 °C. The GC oven temperature was initially held at 170 °C for 10 min, then raised to 200 °C at a rate of 3 °C per min, followed by a further increase to 209 °C at 1.5 °C per min. Helium was used as the carrier gas at a flow rate of 1 mL/min. FAMEs were identified based on retention time and mass spectra using MS-DIAL software (version 4.92), with system suitability assessed using nonadecanoic acid (C19) as internal standard.

Single-nucleus RNA sequencing

The tissue was incubated in TST buffer (146 mM NaCl, 10 mM Tris-Cl pH7.5, 1 mM CaCl2, 21 mM MgCl2, 0.03% Tween-20, 0.01% BSA) at 4 °C for 10 min and then finely minced using Noyes spring scissors. The sample was filtered through a cell strainer and centrifuged at 500 × g for 5 min at 4 °C to remove the supernatant. The nuclear pellet was resuspended in 1% BSA/PBS containing 0.2 U/µl RNase inhibitor and passed through a 30-µm strainer. To quantify nuclei, the suspension was stained with acridine orange and propidium iodide, and counted using the LUNA-FX7 automated cell counter (Logos Biosystems, L70001).

Samples were labeled for multiplexing using the CellPlex reagent. For each sample, $1–2 \times 10^6$ nuclei were resuspended in 100 µl of

CellPlex reagent (10X Genomics, PN-1000261) and incubated at room temperature for 5 min. After labeling, the nuclei were washed three times with 2 ml of cold 1% BSA/PBS and centrifuged at 500 x g for 5 min at 4 °C. Two biological replicate samples were pooled in equal numbers to target the capture of 10,000 nuclei per sample.

Libraries for single cell RNA sequencing were generated using the Chromium Next GEM Single Cell 3'Kit (10X Genomics, PN-1000269), 3'Feature Barcode Kit (10X Genomics, PN-1000262), Dual Index Kit TT Set A (10X Genomics, PN-1000215), and Dual Index Kit NN Set A (10X Genomics, PN-1000243). Nuclei were resuspended in Single Cell Master Mix and loaded into designated wells of the Chromium Next GEM Chip G (10X Genomics, PN-2000127), followed by sequential loading of Gel Beads and Partitioning Oil. GEMs were generated using the Chromium Controller and subjected to reverse transcription in a thermal cycler. After GEM breakage, cDNA was purified using silane magnetic beads and amplified by PCR. During SPRIselect-based size selection, the supernatant and bead fractions were separated to recover barcode DNA from CellPlex oligonucleotides and cDNA derived from polyadenylated mRNA, respectively. For cell multiplexing libraries, 75 µl of the supernatant was retained for additional purification and barcoding PCR using CellPlex primers (10X Genomics, PN-3000482). The bead-bound fraction was processed for gene expression library construction according to the manufacturer's protocol, including fragmentation, end repair, A-tailing, adaptor ligation, and sample index PCR.

Library quality and concentration were assessed using a Bioanalyzer (Agilent). Final libraries were pooled and sequenced on an Illumina HiSeq X Ten platform using a 100 bp paired-end protocol. For 3' gene expression libraries, a minimum sequencing depth of 20,000 read pairs per cell was targeted, while for Cell Multiplexing libraries, a minimum of 5,000 read pairs per cell was aimed.

Single-nucleus RNA sequencing data preprocessing

Raw reads from multiplexed single-nucleus RNA sequencing data derived from gWAT were aligned to the mouse reference genome (GRCm38) and demultiplexed based on sample-specific barcodes using Cell Ranger (v6.1.1). Raw count matrices were generated with cellranger multi, applying the following parameters: min-assignment-confidence = 0.7, expect-cells = 20,000, and include-introns = true. Cells with fewer than 1,000 detected unique molecular identifiers (UMIs) or more than 5% mitochondrial gene content were filtered out for further analysis. Following quality control, count matrices from all samples were merged. Cell clustering was performed using the quickCluster function in the scran (v1.22.1) R package[57], and cell-specific size factors were computed using computeSumFactors function. Normalization was carried out using the logNormCounts function with a pseudo_count = 1. To identify highly variable genes (HVGs), the variance of normalized expression across genes was modeled using modelGeneVar and top HVGs were selected using getTopHVGs function with false discovery rate (FDR) threshold of 0.05. The dataset was then scaled and centered using ScaleData function in Seurat (v4.0.5)[58]. Principal component analysis (PCA) was performed on the HVGs, and batch effects arising from different samples were corrected using RunHarmony function from the harmony (v0.1.0) R package[59]. The top 15 batch-corrected PCs were used for clustering and UMAP dimension reduction. Cluster-specific marker genes were identified using FindAllMarkers function in Seurat, and cell type annotations were manually assigned based on the molecular signatures of each cluster. Putative doublets were detected using the scDblFinder (v1.8.0) R package[60]. These cells were further verified by confirming co-expression of lineage-specific markers and removed. In addition, clusters presumed to originate from adjacent epididymal tissue were annotated based on gene expression: epididymal cells (*Abcb5, Ces5a, Adam7*), spermatozoa (*Dnah12, Spef2, Hydin*) and efferent duct cells (*Adcy8, Dnah5, Slc9a3*), and were excluded from further analysis.

Single-nucleus RNA sequencing data analysis

Differentially expressed genes (DEGs) between TMEM120A AKO and WT mice were identified within adipocytes using FindMarkers function in Seurat R package. Genes with an adjusted P-value < 0.05 and an absolute log2 fold change > 0.25 were considered significant. Functional annotation of DEGs was performed using GO analysis through the DAVID tool (https://david.ncifcrf.gov). To assess the activity of specific metabolic pathways, peroxisome biogenesis (*Pex1, Pex2, Pex3, Pex5, Pex6, Pex7, Pex10, Pex11a, Pex11b, Pex11g, Pex12, Pex13, Pex14, Pex16, Pex19 and Pex26*) and β-oxidation (*Acox1, Acox2, Acox3, Hsd17b4, Ehhadh, Scp2, Abcd1, Abcd2, Abcd3, Cat, Acaa1a, Acaa1b*) scores were calculated using the AddModuleScore function in Seurat. Gene set enrichment analysis (GSEA) was conducted using the fgsea (v1.21.2) R package[61], based on genes ranked by average log2 fold change between TMEM120A AKO and WT within each cell type. Gene sets for GSEA were obtained from Molecular Signatures Database (MsigDB) using the msigdbr (v7.4.1) R package[62]. In addition, TNFα signaling pathway activity in macrophages was inferred using the progeny (v1.16.0) R package[63].

RNA sequencing

Total RNA was extracted from BAT using TRIzol reagent (Thermo Fisher Scientific, cat#15596018) following the manufacturer's instructions. RNA integrity number (RIN), ribosomal RNA (rRNA) ratio, and sample concentration were assessed using an Agilent 2100 Bioanalyzer (Agilent Technologies) with a DNA 1000 chip. For RNA sequencing analysis, cDNA libraries were prepared from 1 µg of total RNA using the TruSeq mRNA Library Kit (Illumina), and sequencing was performed on a NovaSeq 6000 system (Macrogen).

Modeling of mouse TMEM120A-palmitoyl-CoA complex using AlphaFold3

TMEM120A sequences were retrieved from UniProt (human: Q9BXJ8; mouse: Q8C1E7). Using the mouse sequence (Q8C1E7), we employed AlphaFold3 (v3.0) to predict homodimeric TMEM120A complexes with CoA derivatives. Ligand identities were specified via CCD codes (COA for CoA, PKZ for palmitoyl-CoA, 3VV for oleoyl-CoA) under default MSA and template settings. For each ligand, five independent seeds were run (five models per seed, 25 total), and the model with the highest-ranking confidence score was selected for downstream analysis.

Model quality assessment

We evaluated the AlphaFold3–predicted TMEM120A–CoA derivative complex models using three confidence metrics extracted from the pipeline's JSON outputs: pLDDT, Predicted Aligned Error (PAE), and predicted TM-score (pTM). All structures were generated with the AlphaFold3 pipeline under default MSA and template settings. Ligand pLDDT was calculated as the mean pLDDT of all atoms in the CoA derivative chain. Average PAE (protein–ligand) was computed by averaging the PAE matrix entries corresponding to all residue–ligand atom pairs between the TMEM120A chain and the CoA derivative chain. Ligand pTM was determined as the average pTM value reported for the CoA derivative chain. All values are reported to two decimal places.

Statistics

The number of mice used in animal experiments is described within the associated figure legend. GraphPad Prism 9 software (GraphPad Software, USA) was used for statistical analysis. Data are presented as mean ± standard errors of the mean (SEM) as indicated in the Figure

Legends. Statistical significance between two groups was determined by unpaired two-sided Student's t-test. Comparisons among multiple groups were performed using a two-way ANOVA, with Sidak's multiple comparisons test to determine *p* values.

Reporting summary

Further information on research design is available in the Nature Portfolio Reporting Summary linked to this article.

Data availability

All data supporting the findings of this study are available within the article and its Supplementary Information files. Source data are provided with this paper. The raw RNA sequence data reported in this paper have been deposited in the Korea Sequence Read Archive (KRA) under accession code KAP241773. The processed snRNA-seq data of wild-type mouse gonadal white adipose tissue is available at Zenodo [https://doi.org/10.5281/zenodo.17345525][64], which are related to SRA project SRP426501. The publicly available human white adipose tissue snRNA-seq data is available under accession code GSE176171[65]. The raw snRNA-seq data generated in this study have been deposited in the SRA under BioProject accession number PRJNA1271693. The processed file has been deposited in Zenodo and is publicly available at [https://doi.org/10.5281/zenodo.15614282][66]. All microscopy datasets generated in this study have been deposited in Figshare and are publicly available at [https://doi.org/10.6084/m9.figshare.30770492][67]. Source data are provided with this paper.

References

1. Sakers, A., De Siqueira, M. K., Seale, P. & Villanueva, C. J. Adipose-tissue plasticity in health and disease. *Cell* **185**, 419–446 (2022).
2. Cho, Y. K. et al. Lipid remodeling of adipose tissue in metabolic health and disease. *Exp. Mol. Med.* **55**, 1955–1973 (2023).
3. Sharma, A. K., Khandelwal, R. & Wolfrum, C. Futile lipid cycling: from biochemistry to physiology. *Nat. Metab.* **6**, 808–824 (2024).
4. Granneman, J. G., Burnazi, M., Zhu, Z. & Schwamb, L. A. White adipose tissue contributes to UCP1-independent thermogenesis. *Am. J. Physiol. Endocrinol. Metab.* **285**, E1230–1236 (2003).
5. Vaughan, M. The production and release of glycerol by adipose tissue incubated in vitro. *J. Biol. Chem.* **237**, 3354–3358 (1962).
6. Hammond, V. A. & Johnston, D. G. Substrate cycling between triglyceride and fatty acid in human adipocytes. *Metabolism* **36**, 308–313 (1987).
7. Wunderling, K., Zurkovic, J., Zink, F., Kuerschner, L. & Thiele, C. Triglyceride cycling enables modification of stored fatty acids. *Nat. Metab.* **5**, 699–709 (2023).
8. Lynes, M. D. et al. The cold-induced lipokine 12,13-diHOME promotes fatty acid transport into brown adipose tissue. *Nat. Med.* **23**, 631–637 (2017).
9. Cho, Y. K. et al. Adipocyte lysoplasmalogenase TMEM86A regulates plasmalogen homeostasis and protein kinase A-dependent energy metabolism. *Nat. Commun.* **13**, 4084 (2022).
10. Oeckl, J. et al. Loss of UCP1 function augments recruitment of futile lipid cycling for thermogenesis in murine brown fat. *Mol. Metab.* **61**, 101499 (2022).
11. Mottillo, E. P. et al. Coupling of lipolysis and de novo lipogenesis in brown, beige, and white adipose tissues during chronic beta3-adrenergic receptor activation. *J. Lipid Res.* **55**, 2276–2286 (2014).
12. Arner, P. et al. Adipose lipid turnover and long-term changes in body weight. *Nat. Med.* **25**, 1385–1389 (2019).
13. Nagy, H. M. et al. Adipose triglyceride lipase activity is inhibited by long-chain acyl-coenzyme A. *Biochim. Biophys. Acta* **1841**, 588–594 (2014).
14. Coleman, R. A. It takes a village: channeling fatty acid metabolism and triacylglycerol formation via protein interactomes. *J. Lipid Res.* **60**, 490–497 (2019).
15. Ellis, J. M. et al. Adipose Acyl-CoA synthetase-1 directs fatty acids toward β-oxidation and is required for cold thermogenesis. *Cell Metab.* **12**, 53–64 (2010).
16. Sanders, M. A. et al. Endogenous and synthetic ABHD5 ligands regulate ABHD5-perilipin interactions and lipolysis in fat and muscle. *Cell Metab.* **22**, 851–860 (2015).
17. Fiermonte, G., Paradies, E., Todisco, S., Marobbio, C. M. & Palmieri, F. A novel member of solute carrier family 25 (SLC25A42) is a transporter of coenzyme A and adenosine 3′,5′-diphosphate in human mitochondria. *J. Biol. Chem.* **284**, 18152–18159 (2009).
18. Agrimi, G., Russo, A., Scarcia, P. & Palmieri, F. The human gene SLC25A17 encodes a peroxisomal transporter of coenzyme A, FAD and NAD+. *Biochem. J.* **443**, 241–247 (2012).
19. Niu, Y. et al. Analysis of the mechanosensor channel functionality of TACAN. *Elife* **10**, e71188 (2021).
20. Rong, Y. et al. TMEM120A contains a specific coenzyme A-binding site and might not mediate poking- or stretch-induced channel activities in cells. *Elife* **10** (2021).
21. Xue, J. et al. TMEM120A is a coenzyme A-binding membrane protein with structural similarities to ELOVL fatty acid elongase. *Elife* 10 (2021).
22. Batrakou, D. G., de Las Heras, J. I., Czapiewski, R., Mouras, R. & Schirmer, E. C. TMEM120A and B: nuclear envelope transmembrane proteins important for adipocyte differentiation. *PLoS One* **10**, e0127712 (2015).
23. Beaulieu-Laroche, L. et al. TACAN is an ion channel involved in sensing mechanical pain. *Cell* **180**, 956–967.e917 (2020).
24. Ohno, Y. et al. ELOVL1 production of C24 acyl-CoAs is linked to C24 sphingolipid synthesis. *Proc. Natl. Acad. Sci. USA* **107**, 18439–18444 (2010).
25. Tamura, K. et al. Novel lipogenic enzyme ELOVL7 is involved in prostate cancer growth through saturated long-chain fatty acid metabolism. *Cancer Res.* **69**, 8133–8140 (2009).
26. Huh, J. Y. et al. TANK-binding kinase 1 regulates the localization of acyl-CoA synthetase ACSL1 to control hepatic fatty acid oxidation. *Cell Metab.* **32**, 1012–1027 e1017 (2020).
27. Poppelreuther, M. et al. The metabolic capacity of lipid droplet localized acyl-CoA synthetase 3 is not sufficient to support local triglyceride synthesis independent of the endoplasmic reticulum in A431 cells. *Biochim. Biophys. Acta (BBA) Mol. Cell Biol. Lipids* **1863**, 614–624 (2018).
28. Poppelreuther, M. et al. The N-terminal region of acyl-CoA synthetase 3 is essential for both the localization on lipid droplets and the function in fatty acid uptake. *J. Lipid Res.* **53**, 888–900 (2012).
29. Klasson, T. D. et al. ACSL3 regulates lipid droplet biogenesis and ferroptosis sensitivity in clear cell renal cell carcinoma. *Cancer Metab.* **10**, 14 (2022).
30. Cooper, D. E., Young, P. A., Klett, E. L. & Coleman, R. A. Physiological consequences of compartmentalized Acyl-CoA metabolism. *J. Biol. Chem.* **290**, 20023–20031 (2015).
31. Chitraju, C. et al. Triglyceride synthesis by DGAT1 protects adipocytes from lipid-induced ER stress during lipolysis. *Cell Metab.* **26**, 407–418 e403 (2017).
32. Zeeshan, H. M., Lee, G. H., Kim, H. R. & Chae, H. J. Endoplasmic reticulum stress and associated ROS. *Int. J. Mol. Sci.* **17**, 327 (2016).
33. Mottillo, E. P. et al. A FRET sensor for the real-time detection of long chain acyl-CoAs and synthetic ABHD5 ligands. *Cell Rep. Methods* **3**, 100394 (2023).
34. Rondini, E. A. et al. Novel pharmacological probes reveal ABHD5 as a locus of lipolysis control in white and brown adipocytes. *J. Pharm. Exp. Ther.* **363**, 367–376 (2017).

35. Czapiewski, R. et al. Genomic loci mispositioning in Tmem120a knockout mice yields latent lipodystrophy. *Nat. Commun.* **13**, 321 (2022).
36. Malik, P. et al. Cell-specific and lamin-dependent targeting of novel transmembrane proteins in the nuclear envelope. *Cell Mol. Life Sci.* **67**, 1353–1369 (2010).
37. de las Heras, J. I. et al. Tissue-specific NETs alter genome organization and regulation even in a heterologous system. *Nucleus* **8**, 81–97 (2017).
38. Li, S. et al. Gain-of-function genetic screening identifies the antiviral function of TMEM120A via STING activation. *Nat. Commun.* **13**, 105 (2022).
39. Hunt, M. C. & Alexson, S. E. H. The role Acyl-CoA thioesterases play in mediating intracellular lipid metabolism. *Prog. Lipid Res.* **41**, 99–130 (2002).
40. Bekeova, C. et al. Multiple mitochondrial thioesterases have distinct tissue and substrate specificity and CoA regulation, suggesting unique functional roles. *J. Biol. Chem.* **294**, 19034–19047 (2019).
41. Bu, S. Y. & Mashek, D. G. Hepatic long-chain acyl-CoA synthetase 5 mediates fatty acid channeling between anabolic and catabolic pathways[S]. *J. Lipid Res.* **51**, 3270–3280 (2010).
42. Sharma, A. K. et al. Basal re-esterification finetunes mitochondrial fatty acid utilization. *Mol. Metab.* **71**, 101701 (2023).
43. Lobo, S., Wiczer, B. M. & Bernlohr, D. A. Functional analysis of long-chain acyl-CoA synthetase 1 in 3T3-L1 adipocytes. *J. Biol. Chem.* **284**, 18347–18356 (2009).
44. Li, L. O. et al. Liver-specific loss of long chain Acyl-CoA synthetase-1 decreases triacylglycerol synthesis and β-oxidation and alters phospholipid fatty acid composition*. *J. Biol. Chem.* **284**, 27816–27826 (2009).
45. Young, P. A. et al. Long-chain acyl-CoA synthetase 1 interacts with key proteins that activate and direct fatty acids into niche hepatic pathways. *J. Biol. Chem.* **293**, 16724–16740 (2018).
46. Jiang, S. et al. Unveiling the crucial role of peroxisomal acyl-CoA metabolism in muscle atrophy: Insights from genetic models and therapeutic interventions. *Nano Today* **58**, 102417 (2024).
47. Listenberger, L. L. et al. Triglyceride accumulation protects against fatty acid-induced lipotoxicity. *Proc. Natl. Acad. Sci.* **100**, 3077–3082 (2003).
48. Roesler, A. & Kazak, L. UCP1-independent thermogenesis. *Biochem. J.* **477**, 709–725 (2020).
49. Stanic, S. et al. Prolonged FGF21 treatment increases energy expenditure and induces weight loss in obese mice independently of UCP1 and adrenergic signaling. *Biochem. Pharmacol.* **221**, 116042 (2024).
50. Natarajan, D. et al. Chronic β3-AR stimulation activates distinct thermogenic mechanisms in brown and white adipose tissue and improves systemic metabolism in aged mice. *Aging Cell* **23**, e14321 (2024).
51. Galarraga, M. et al. Adiposoft: automated software for the analysis of white adipose tissue cellularity in histological sections. *J. Lipid Res.* **53**, 2791–2796 (2012).
52. Neubauer, S. et al. LC-MS/MS-based analysis of coenzyme A and short-chain acyl-coenzyme A thioesters. *Anal. Bioanal. Chem.* **407**, 6681–6688 (2015).
53. Matyash, V., Liebisch, G., Kurzchalia, T. V., Shevchenko, A. & Schwudke, D. Lipid extraction by methyl-tert-butyl ether for high-throughput lipidomics. *J. Lipid Res.* **49**, 1137–1146 (2008).
54. Shim, M. et al. Histone demethylase inhibitor KDM5-C70 regulates metabolomic and lipidomic programming during an astrocyte differentiation of rat neural stem cell. *Sci. Rep.* **15**, 5409 (2025).
55. Lee, D.-K. et al. In vitro tracking of intracellular metabolism-derived cancer volatiles via isotope labeling. *ACS Cent. Sci.* **4**, 1037–1044 (2018).
56. Kim, S. J. et al. Exposure to nano-polystyrene induces metabolic alteration in lipid homeostasis in Caco-2. *Environ. Sci. Nano* **8**, 1408–1424 (2021).
57. Lun, A. T., McCarthy, D. J. & Marioni, J. C. A step-by-step workflow for low-level analysis of single-cell RNA-seq data with Bioconductor. *F1000Res* **5**, 2122 (2016).
58. Butler, A., Hoffman, P., Smibert, P., Papalexi, E. & Satija, R. Integrating single-cell transcriptomic data across different conditions, technologies, and species. *Nat. Biotechnol.* **36**, 411–420 (2018).
59. Korsunsky, I. et al. Fast, sensitive and accurate integration of single-cell data with Harmony. *Nat. Methods* **16**, 1289–1296 (2019).
60. Germain, P. L., Lun, A., Garcia Meixide, C., Macnair, W. & Robinson, M. D. Doublet identification in single-cell sequencing data using scDblFinder. *F1000Res* **10**, 979 (2021).
61. Korotkevich, G. et al. Fast gene set enrichment analysis. *bioRxiv*, 060012 (2021).
62. Castanza, A. S. et al. Extending support for mouse data in the Molecular Signatures Database (MSigDB). *Nat. Methods* **20**, 1619–1620 (2023).
63. Schubert, M. et al. Perturbation-response genes reveal signaling footprints in cancer gene expression. *Nat. Commun.* **9**, 20 (2018).
64. Jeong, Y.L. Single-nucleus RNA sequencing data of mice gonadal white adipose tissue (WT NCD, WT HFD, Tm4sf19 KO NCD, Tm4sf19 KO HFD). Zenodo. https://doi.org/10.5281/zenodo.17345525 (2024).
65. Emont, M. P. et al. A single-cell atlas of human and mouse white adipose tissue. *Nature* **603**, 926–933 (2022).
66. Jeong, Y.L. Single-nucleus RNA sequencing data of mice gonadal white adipose tissue (WT NCD and Tmem120a KO). Zenodo. https://doi.org/10.5281/zenodo.15614282 (2025).
67. Lee, J. et al. Microscopy image dataset for analyzing TMEM120A localization, interactions, and metabolic function in adipose tissue. Figshare. https://doi.org/10.6084/m9.figshare.30770492 (2025).

Acknowledgements

This research was supported by National Research Foundation of Korea grants (RS-2023-00213572 and RS-2024-00400118 to Y.-H.L.; NRF-2022R1A6A3A13071509 to Y.K.C.; NRF-2021M3H9A1030158 to J.K.K), by the Bio&Medical Technology Development Program of the National Research Foundation (NRF) funded by the Korean government (MSIT) (RS-2025-16063709 to Y.-H.L.), and by US NIH grants (R01-DK76229 and R01-DK62292 to J.G.G.).

Author contributions

Y.-H.L., Y.K.C., and J.G.G. conceived and designed the study. Y.K.C., J.K.S., Y.-S.J. and J.L.(Junhyuck) conducted the in vivo and in vitro experiments. Y.L.J., Y.H.C., and J.K.K. performed snRNA-seq analysis. M.S. and D.-K.L. conducted FA re-esterification analysis. X.L.M. and S.P. conducted FA elongation activity analysis. C.J. and S.W.K. performed FAME analysis in vivo. C.S. and J.L.(Juyong) analyzed structure prediction. S.N. provided human samples. Y.K.C. analyzed human samples. Y.K.C., E.M., and J.G.G. analyzed ABHD5-PLIN5 FRET assay. Y.-H.L., Y.K.C., J.L.(Junhyuck), and J.G.G wrote the manuscript. All authors reviewed the manuscript.

Competing interests

The authors declare no competing interests.

Additional information

Supplementary information The online version contains supplementary material available at https://doi.org/10.1038/s41467-025-67870-7.

Correspondence and requests for materials should be addressed to Dong-Kyu Lee, Jong Kyoung Kim or Yun-Hee Lee.

Peer review information *Nature Communications* thanks Martin Klingenspor who co-reviewed with Silas Wisser and the other anonymous, reviewer(s) for their contribution to the peer review of this work. A peer review file is available.

Reprints and permissions information is available at http://www.nature.com/reprints

Publisher's note Springer Nature remains neutral with regard to jurisdictional claims in published maps and institutional affiliations.

Open Access This article is licensed under a Creative Commons Attribution-NonCommercial-NoDerivatives 4.0 International License, which permits any non-commercial use, sharing, distribution and reproduction in any medium or format, as long as you give appropriate credit to the original author(s) and the source, provide a link to the Creative Commons licence, and indicate if you modified the licensed material. You do not have permission under this licence to share adapted material derived from this article or parts of it. The images or other third party material in this article are included in the article's Creative Commons licence, unless indicated otherwise in a credit line to the material. If material is not included in the article's Creative Commons licence and your intended use is not permitted by statutory regulation or exceeds the permitted use, you will need to obtain permission directly from the copyright holder. To view a copy of this licence, visit http://creativecommons.org/licenses/by-nc-nd/4.0/.

© The Author(s) 2025